



Precision control of miniature SCARA robots for multi-object spectrographs

Luzius Kronig, Philipp Hörler, Stefane Caseiro, Loic Grossen, Ricardo Araujo, Jean-Paul Kneib & Mohamed Bouri

To cite this article: Luzius Kronig, Philipp Hörler, Stefane Caseiro, Loic Grossen, Ricardo Araujo, Jean-Paul Kneib & Mohamed Bouri (2020) Precision control of miniature SCARA robots for multi-object spectrographs, International Journal of Optomechatronics, 14:1, 53-77, DOI: [10.1080/15599612.2020.1829218](https://doi.org/10.1080/15599612.2020.1829218)

To link to this article: <https://doi.org/10.1080/15599612.2020.1829218>



© 2020 The Author(s). Published with license by Taylor & Francis Group, LLC



Published online: 10 Dec 2020.



Submit your article to this journal [↗](#)



Article views: 669



View related articles [↗](#)




View Crossmark data [↗](#)



Citing articles: 1 View citing articles [↗](#)

Precision control of miniature SCARA robots for multi-object spectrographs

Luzius Kronig , Philipp Hörler, Stefane Caseiro, Loic Grossen, Ricardo Araujo, Jean-Paul Kneib, and Mohamed Bourri

Ecole Polytechnique Fédérale de Lausanne, REHASSIST-LASTRO, Lausanne, Switzerland

ABSTRACT

Advances in astronomy led to the demand for measuring the spectra of multiple night sky objects simultaneously. Some of these Multi-Object Spectrographs use robotic systems that position optical fibers in the focal plane of the observing telescope. These systems rely on precise fiber placement in order to collect the light spectra of faint stars and galaxies. Here, we present how to design, control, and operate micro SCARA-like robots to position optical fibers to micrometer precision. As an illustrative example, we show the design and performance results of the SDSS-V fiber positioner, which has been build for the Apache Point Observatory and the Las Campanas Observatory with 500 units for each telescope.

KEYWORDS

Fiber positioner; control; calibration; multi-object spectrograph; MOS; massive spectroscopy; metrology; characterization; position; calibration; validation; SCARA robot

1. Introduction

The light spectrum emitted by stars, galaxies, and quasars contains an abundance of information for astronomic research. Properties such as chemical composition, distance, luminosity, temperature, and other parameters can be derived from the analysis of the spectrum of the objects. In recent years significant efforts have been made to develop telescopes that can measure a significant number of light spectra in parallel.^[1–9] With these telescopes, called Multi-Object Spectrographs, astronomers try to measure a maximum of targets in parallel, in order to study, for example, the mystery of dark energy, the history of the milky way, or the evolution of super-massive black holes. Different solutions to capture the light of multiple galaxies, quasars and stars in parallel exist.^[10–14] One promising approach is to use optical fibers (Figure 1). A section of the night sky is projected onto the focal plane of an earth-based telescope. The spectrum of a star or galaxy is then measured by placing an optical fiber on the corresponding spot in the focal plane. The optical fiber transmits the captured photons to the spectrograph, which measures the light spectrum with high resolution. After the measurement, the fiber can be repositioned to a new target. In order to measure many targets in parallel, the number of fibers is maximized. The correct placement of the optical fibers can be achieved with miniature SCARA Robots^[15–25] (Figures 2 and 3). These robots have two serially actuated rotation axes (α and β), which position the fibers with micrometer precision on the focal plane. The standard forward and backward kinematic of the planar RR part of SCARA robots applies:

$$\mathbf{r}_{target} = \mathcal{P} \begin{pmatrix} \alpha \\ \beta \end{pmatrix} = \mathbf{r}_{center} + l_a \begin{pmatrix} \cos(\alpha + \alpha_{off}) \\ \sin(\alpha + \alpha_{off}) \end{pmatrix} + l_b \begin{pmatrix} \cos(\alpha + \alpha_{off} + \beta) \\ \sin(\alpha + \alpha_{off} + \beta) \end{pmatrix} \quad (1)$$

CONTACT Luzius Kronig  luzius.kronig@epfl.ch  Ecole Polytechnique Fédérale de Lausanne, REHASSIST-LASTRO, CH-1015, Lausanne, Switzerland

© 2020 The Author(s). Published with license by Taylor & Francis Group, LLC

This is an Open Access article distributed under the terms of the Creative Commons Attribution License (<http://creativecommons.org/licenses/by/4.0/>), which permits unrestricted use, distribution, and reproduction in any medium, provided the original work is properly cited.

Nomenclature

\mathbf{r}_{target}	x,y coordinates of the optical fiber in the focal plane	δ_θ	angle indicating the deviation from a linear reduction ratio
\mathbf{r}_{center}	x,y coordinates of the center of the positioner	$\tilde{\theta}_s$	output angles corresponding to discretely spaced motor positions θ_{motor_s}
l_a	alpha arm length	T_{cog}	motor cogging torque
l_b	beta arm length	F_{BEMF}	back electromotive force (BEMF) torque acting on motor
α	alpha arm rotation angle	$F_{friction}$	friction torque of rotation axis
β	beta arm rotation angle	T_{spring}	torque exerted from play reduction spring
θ	vector representing the angular orientation of both axes	T_{ba}	break-away torque
θ	rotation angle at the output of the axis representing a general substitute for either α or β	u	voltage
\mathcal{P}	forward kinematic function	R	coil resistance
p	distance between the centers of two neighboring positioners	i	coil current
T_{motor}	motor torque	\mathbf{L}	matrix containing self and mutual inductances
θ_{motor}	motor angle	λ	total flux linkage
\bar{n}	average transmission ratio	λ_{PM}	flux linkage of the permanent magnet
B	backlash	Σ_{meas}	covariance matrix containing the measurement uncertainties of the measured fiber position \mathbf{r}_{meas}
\mathcal{T}	function describing the relation between θ_{motor} and θ	Σ_{cmd}	covariance matrix containing the uncertainties of the commanded fiber position \mathbf{r}_{cmd}

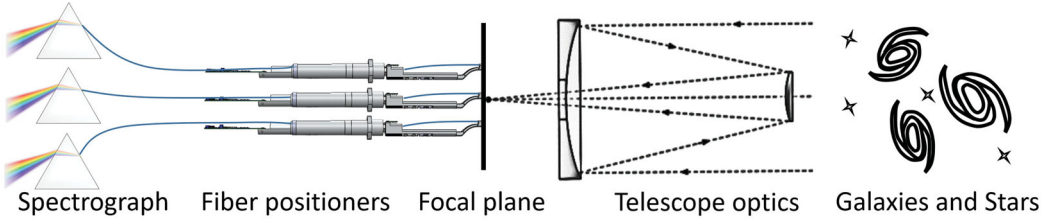


Figure 1. Principle of multi-object spectroscopy (adapted from^[15]).

$$\theta = \begin{pmatrix} \alpha \\ \beta \end{pmatrix} = \mathcal{P}^{-1}(\mathbf{r}_{target}) = \begin{pmatrix} \text{atan2}(\mathbf{r}_{target} - \mathbf{r}_{center}) - \cos^{-1}\left(\frac{\|\mathbf{r}_{target} - \mathbf{r}_{center}\|^2 + l_a^2 - l_b^2}{2l_a\|\mathbf{r}_{target} - \mathbf{r}_{center}\|}\right) - \alpha_{off} \\ \cos^{-1}\left(\frac{\|\mathbf{r}_{target} - \mathbf{r}_{center}\|^2 - l_a^2 - l_b^2}{2l_al_b}\right) \end{pmatrix} \quad (2)$$

The vector \mathbf{r}_{target} represents the x, y coordinates of the target in the focal plane, and has to be defined within the workspace of the positioner. The vector \mathbf{r}_{center} points to the center of the positioner and α_{off} is its orientation with regards to the reference frame of the focal plane. The arm lengths l_a and l_b as well as the rotation angles α and β are defined as shown in Figure 2. In this paper, we use a bold θ to represent the angular orientation (α and β) for both axes. θ represents a general substitute for either of the two axes.

The main challenge consists of respecting the maximal allowable positioning error. Misplacing the fiber in the focal plane leads to a loss of light. Typically, the used fibers have a light-transmissive core with a diameter of about 100 μm . The maximum allowable x, y positioning error is telescope specific and depends on the fiber core diameter and the size of the object in the focal plane. The positioning requirement is in general around 4% of the actual core diameter.^[27] Table 1 shows the maximal

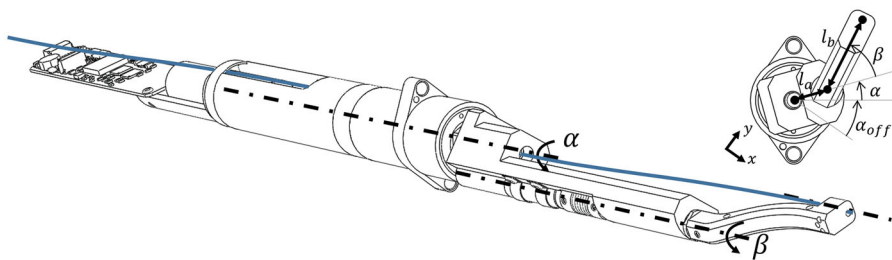


Figure 2. Sketch of the fiber positioner of the SDSS-V project with rotation axis α and β with arm lengths l_a and l_b . The optical fiber (blue) is fixed at the end of the beta arm. (adapted from^[26]).

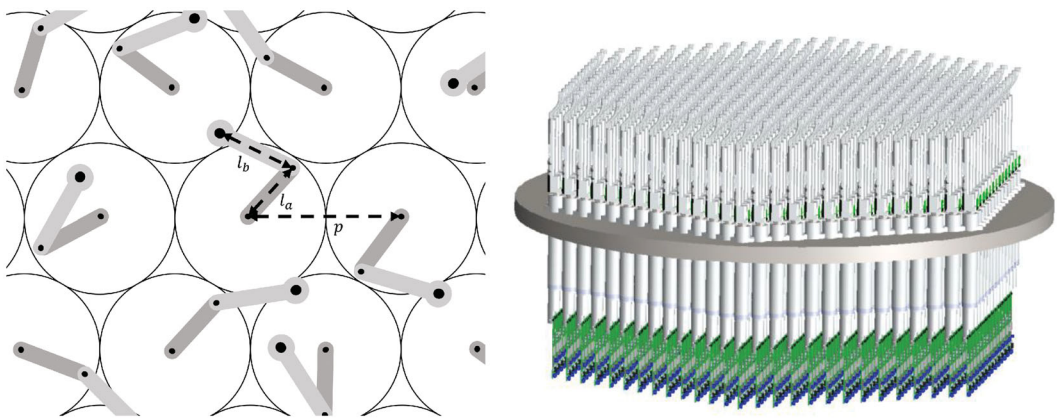


Figure 3. Left: overlapping workspace, Right: robot distribution in the focal plane (adapted from^[15]).

Table 1. Overview of alpha-beta positioners.

Positioner	Units	Alpha [mm]	Beta [mm]	Pitch [mm]	Abs. position requirement	Actuation	Metrology System	Year
LAMOST ^[2]	4000	8.25	8.25	25.6	40 [μm] max	Stepper	Yes	2012
MEGARA ^[3,28]	92	5.803	5.803	20.1	102 [μm] max	Stepper	No	2017
DES ^[19,20,29,30]	5000	3	3	10.4	5 [μm] max	BLDC	Yes	2020
SDSS-V	2 × 500	7.4	15	22.4	5 [μm] max	BLDC	Yes	2020
MOONS ^[5,16,31]	1001	8	17	25	20 [μm] max	Stepper	Yes*	2020
COBRA ^[17,18]	2400	2.375	2.375	8	5 [μm] max	Piezo	Yes	2020

*not intended to be used during observations.

allowable position error requirement for all commissioned or planned instruments with alpha-beta positioners to date. Note that SDSS-V has the most stringent angular requirement of the actuator due to the low position requirement of 5 μm combined with a long stretched out arm length of 22.4 mm. The table shows also that alpha-beta instruments with stringent position requirement below 20 μm are either still in commissioning phase or in construction as of 2020.

Without a dedicated metrology system for repositioning, both, a good repeatability and an absolute position accuracy of the positioner are needed to guarantee the positioning requirement of the instruments. This is the case for MOONS and MEGARA with a positioning requirement of 20 and 102 μm, respectively. The other listed telescopes use a metrology camera to verify the correct location of the fiber tips.^[28,29,32] One or more cameras take a picture of the entire focal plane, and image processing software determines the accurate position of every fiber tip. These measurements can then be used to correct for the uncertainties in the positioner model.

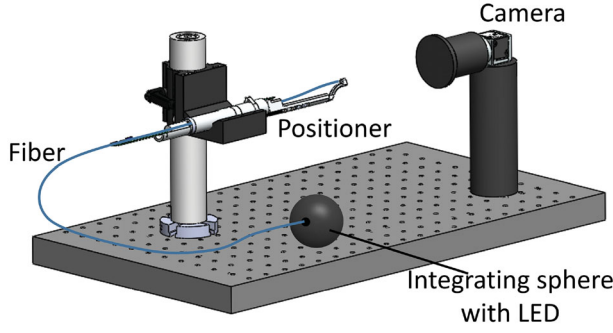


Figure 4. A robot is set up with an optical fiber that is back-illuminated with a LED. An integrating sphere ensures an even intensity distribution of the light exiting the fiber tip. A camera positioned in front of the positioner takes an image of its workspace and image processing calculates then accurately the x, y location of the fiber end by determining the center of the measured light spot.

Therefore, the absolute positioning error is only limited by their repeatability, allowing for more stringent error requirements.

For our measurements, we used a similar metrology system already introduced in previous work^[26,33] (Figure 4). A robot is set up with an optical fiber that is back-illuminated with a LED. An integrating sphere ensures an even intensity distribution of the light exiting the fiber tip. A camera positioned in front of the positioner takes an image of its workspace and image processing calculates then accurately the x, y location of the fiber end by determining the center of the measured light spot. This set up is used to calibrate the positioner, assess its performance, and emulate its operating mode in the telescope.

In the following, we show how a high positioning accuracy can be achieved by design, control, and calibration without the need for bulky angular encoders. We also introduce a collision detection algorithm based on the derived controller. As an example, we show the design and performance results of the SDSS-V positioner build for the 2.5 m Sloan Telescope at the Apache Point Observatory in the USA and the 2.5 m Irénée du Point Telescope at the Las Campanas Observatory in Chile with an alpha and beta arm length of 7.4 and 15 mm, respectively (Figure 2) with 500 units for each telescope.

2. Positioner

In this section, we show the positioner's design aspects, the physical behavior and some measurement results validating the model.

2.1. Design

Figure 4 shows the distribution of the robots in the focal plane. The pitch p is defined as the distance between the centers of two neighboring positioners. The positioners are densely packed. The total number of required optical fibers defines how to distribute the positioners, and how to choose the alpha and beta arm lengths. A hexagonal distribution pattern allows us to maximize the available space for the mechanical design of the positioners. The workspaces of the units can overlap, so that multiple positioners can reach a single target. SDSS-V has 500 fibers feeding the BOSS spectrograph (wavelength range: 0.36–1.04 μm) and 300 fibers for the APOGEE spectrograph (wavelength range: 1.51–1.70 μm). That means that a subset of 300 positioners is equipped with both fibers. The goal is to choose the arm lengths such that full coverage is possible for both fiber types. In general, a full coverage of the focal plane can either be reached by choosing an equal length for both arms ($l_a = l_b$) or by ensuring that every positioner can reach the center

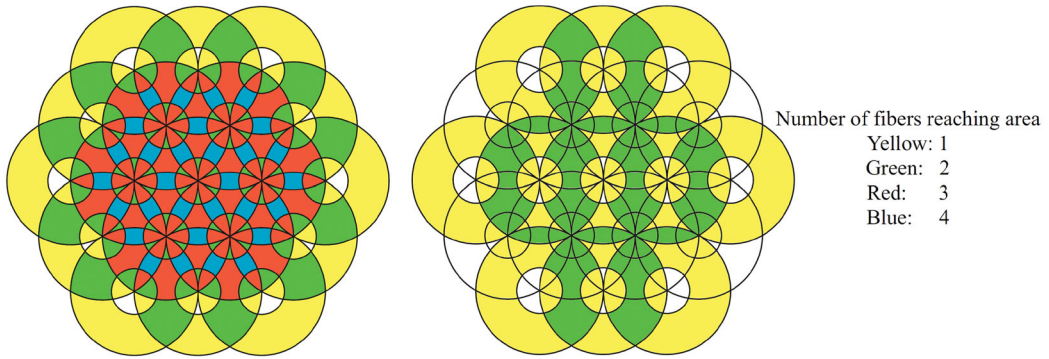


Figure 5. The figure shows how many fibers can reach a certain location in the focal plane. Here, the arm lengths are chosen such that every positioner can reach the center of its neighbours ($p = l_a + l_b$). Left: coverage if every positioner is equipped with one optical fiber. Right: coverage if only every second positioner is equipped with an optical fiber. (adapted from^[27]).

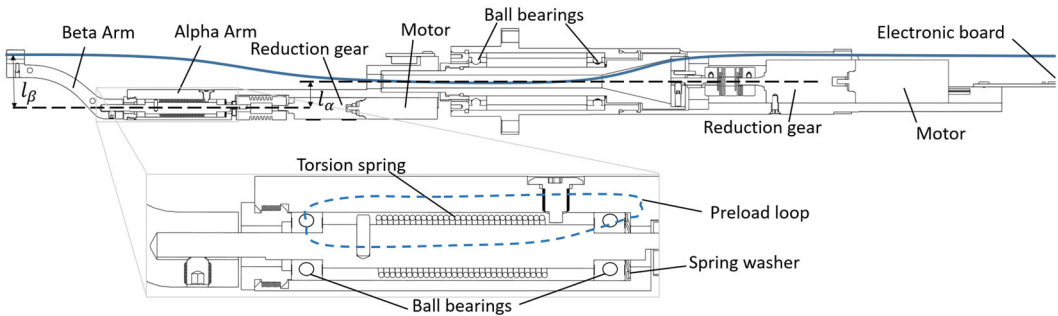


Figure 6. Cross section of the fiber positioner. A close up of the beta axis shows the preloaded bearings and the play reducing torsion spring.

of its neighbors ($p = l_a + l_b$).^[27] SDSS-V chose the second option for its 500 positioners (Figure 5) because it allows us to almost reach full focal plane coverage for either kind of fiber. Between two observations, the optical fibers move to the new target galaxies or stars, whereas the arms of neighboring robots should not collide. Careful path planning, with collision avoidance algorithms, prevents clashing of the positioners.^[34–37] As the robots are limited in diameter, the available space in length is exploited. Figure 6 shows a cross-section of a single positioner. The fiber is fixed on the beta arm and guided through a hollow rotation axis of the alpha arm. This guidance allows for minimizing the bending of the fiber to prevent light throughput loss.

A challenge of the design is not only the high position accuracy but also the correct alignment of the fibers, since a misalignment of the fiber tip also induces a loss of light. The alignment axis of the fiber tips should point to the common focal point of the focal plane. Design and manufacturing tolerances guarantee the correct fiber alignment, and the alignment is, therefore, not actively controlled. Ball bearings guarantee the strict alignment of the rotation axes. The ball bearings are spaced so far apart that manufacturing tolerances have a negligible effect on the correct axis alignment. Additionally, the ball bearings have to be preloaded in order to prevent wobbling and to ensure that the axes run in a perfect circular motion. During an observation, the robots do not move. The whole telescope, on the other hand, moves to compensate for the rotation of the Earth. This tracking leads to a rotation of the gravity vector, which acts on the positioner. Therefore, a stiff positioner design prevents the flecion of the positioner due to its self-weight or other external disturbance forces.

High precisions can be achieved with a precise sensor at the output shaft of the rotation axis. However, for this specific application with limited available space, no such affordable sensors with high enough accuracy exist. An angular resolution of about 0.02 degrees with an actuator diameter of not more than 4–6 mm is needed. Here, instead of a sensor, the reduction gear guarantees the positioning accuracy. An angle inaccuracy on the motor side is divided by the reduction ratio and yields a much smaller angular error at the output. The positioning accuracy is, however, limited by a not constant reduction ratio, play, and the compliance of the gear. The reduction is chosen such that the required precision at the output shaft is reached. For example, with a motor inaccuracy of 5 degrees and a required precision at the output shaft of 0.01 degrees, a reduction ratio of minimum 1:500 is needed. Furthermore, the ratio is chosen such that the gear is not back drivable through externally applied forces and torques.

In order to guarantee a stable position, the output of the gear must not have any play. As the workspace is not more than one full rotation at the gear output, a torsion spring can eliminate the play, such as shown in the close up of [Figure 6](#). The torsional stress cannot be maintained all the way to the motor since it would render the gear back drivable. A combination of friction and decrease in torque due to the gear reduction results in the elimination of the play only for the last reduction stages. Therefore, a small play persists in the first stages after the motor. The torque of the spring must be stronger than the external disturbance forces and, at the same time, smaller than the total friction of the gear.

Finally, attention must be paid to keep the cross-sectional area small, as the number of fibers is fixed for a given size of the focal plane ([Figure 4](#)). The focal plane of such telescopes has a diameter of about 1000 mm, with a fiber density between 500 and 5000 fibers per plane. The maximum pitch p lies, therefore, between 7 and 25 mm. For future telescopes, the fiber-density will likely increase, and robots with even smaller cross-sectional areas will be required.

2.2. Drivetrain model

One rotation axis of the positioner can be modeled, such as shown in [Figure 7](#). A brushless DC motor acts with torque T_{motor} on the rotation axis with motor inertia J_{motor} . The motor shaft drives the reduction gear, which consists of serially linked reduction stages. A cogwheel pairing represents the model of each reduction stage with backlash B_i , friction F_i , compliance k_i , Inertia J_i , and a reduction factor n_i . The gear drives the output inertia J_{out} with angle θ which also receives a torque by the torsion spring. The torsion spring closes the backlash for the last reduction stages,

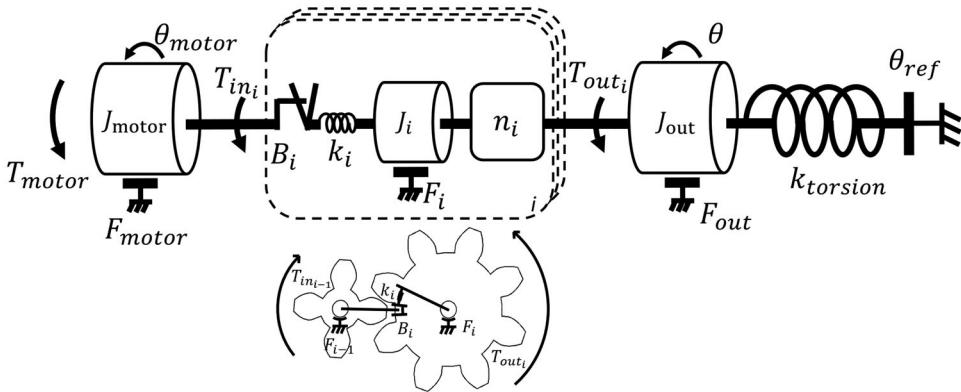


Figure 7. The drivetrain model of one axis is depicted. The motor torque T_{motor} acts on the rotation axis with motor inertia J_{motor} . The motor shaft drives the reduction gear, which consists of serially linked reduction stages. A cogwheel pairing represents the model of each reduction stage with backlash B_i , friction F_i , compliance k_i , Inertia J_i , and a reduction factor n_i . The gear drives the output inertia J_{out} with angle θ , which also receives a torque by the torsion spring.

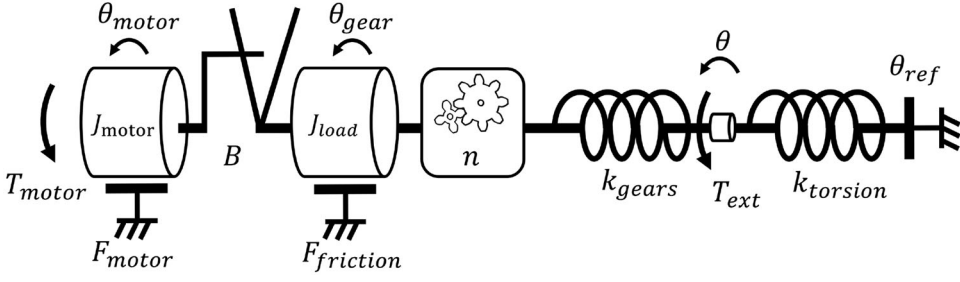


Figure 8. The simplified drivetrain model is reduced to a two body system with inertias J_{motor} and J_{load} . The reduction gear is represented with a single backlash opening B , friction $F_{friction}$, and compliance k_{gear} . n represents the overall reduction ratio.

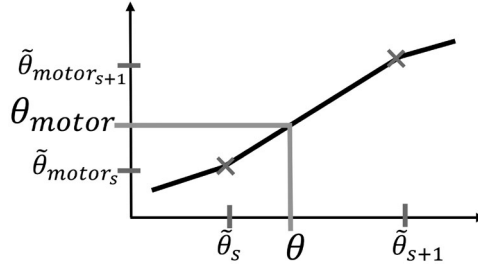


Figure 9. The non-linear transmission is calibrated by measuring different output angles $\tilde{\theta}_s$ with commanded motor positions $\tilde{\theta}_{motor_s}$. A simple linear interpolation connects the calibrated points.

and therefore we can simplify the model to a single backlash opening just after the motor. This allows us to simplify the model further by grouping the inertia, friction, compliance, and reduction ratio of the reduction gear to a single inertia J_{load} , compliance k_{gear} and friction $F_{friction}$. The overall reduction ratio is denoted as n (Figure 8).

With the simplified model, we can distinguish between the two cases where the motor is either within the backlash gap or where the gap is closed and the motor is in full contact with the reduction gear. Equation 3 shows the equation of motion for the case, where the backlash is closed. The motor can either be in positive or negative contact, whereas the motor angle θ_{motor} is offset by the backlash B from the gear angle θ_{gear} in case of positive contact. Since we assume that the gear is not back drivable, positive contact is maintained as long as the motor output torque stays positive: $T_{motor} - F_{motor} > 0$. Idem applies for a negative contact: $T_{motor} - F_{motor} < 0$.

$$\ddot{\theta}_{motor}(J_{motor} + J_{load}) = T_{motor} - F_{motor} - F_{friction} - nk_{torsion}(\theta - \theta_{ref}) - nT_{ext} \quad (3a)$$

$$\text{positive contact : } \theta_{motor} = \theta_{gear} - B \quad (3b)$$

$$\text{negative contact : } \theta_{motor} = \theta_{gear} \quad (3c)$$

Once the motor transitions into the backlash, the system splits into two independent equations of motion one for the gear and one for the motor. The system stays within the backlash as long as $|\theta_{gear} - \theta_{motor}| < B$:

$$\ddot{\theta}_{gear}J_{load} = -F_{friction} - nk_{torsion}(\theta - \theta_{ref}) - nT_{ext} \quad (4a)$$

$$\ddot{\theta}_{motor}J_{motor} = T_{motor} - F_{motor} \quad (4b)$$

In any of the two cases, the angular position at the output depends on the gear ratio n , the external disturbance torque T_{ext} and the total compliance $k = k_{gears} + k_{torsion}$ of the gear:

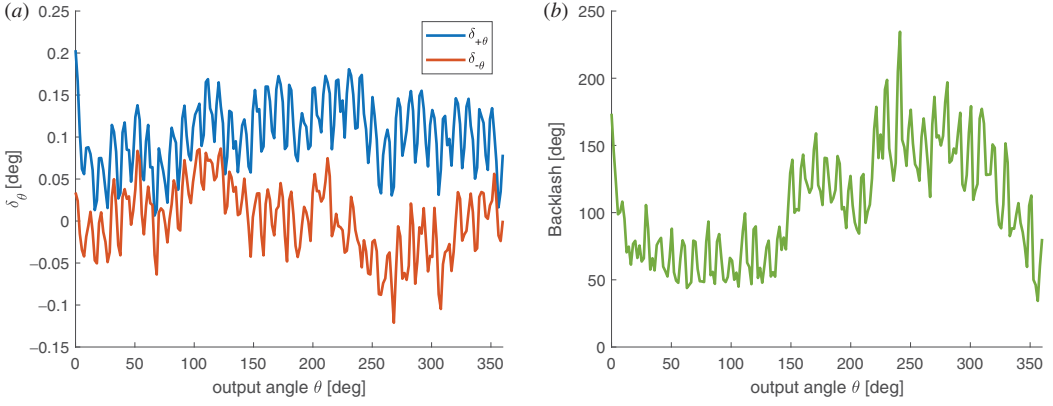


Figure 10. Left: the figure shows the deviation δ_θ from a linear reduction ratio for the positive and negative gear contact. Right: the figure shows the measured backlash in the planetary gear depending on the output angle θ .

$$\theta = \theta_{gear}/n + T_{ext}/k \quad (5a)$$

2.3. Non-linear transmission and backlash

The reduction ratio depends on the radius and shape of the gear teeth pairing of each reduction stage. The teeth radius and shape are slightly different for every tooth pairing, and hence, the reduction ratio n depends on the angle θ . Additionally, the exact reduction ratio depends on whether the motor is in positive or negative contact. Therefore the backlash B is likewise a function of θ . Neglecting external forces T_{ext} we can define a function \mathcal{T} which describes the relation between θ_{motor} and θ . For a negative backlash contact, we define $\theta_{motor} = \mathcal{T}_-(\theta) = n \cdot \theta$, and similarly $\theta_{motor} = \mathcal{T}_+(\theta) = n \cdot \theta + B$ for a positive contact. We can measure and calibrate the exact relation between θ_{motor} and θ by driving the motor to a fixed number of discretely spaced motor positions $\tilde{\theta}_{motor}$ and measuring the corresponding output position $\tilde{\theta}$ (see Figure 9). We use a linear interpolation to approximate any motor angles within the measurement points:

$$\theta_{motor} = \mathcal{T}(\theta) = \tilde{\theta}_{motor_s} + (\theta - \tilde{\theta}_s) \frac{\tilde{\theta}_{motor_{s+1}} - \tilde{\theta}_{motor_s}}{\tilde{\theta}_{s+1} - \tilde{\theta}_s} \text{ for } \tilde{\theta}_s < \theta \leq \tilde{\theta}_{s+1} \quad (6)$$

For better illustration of this nonlinear behaviour, we can calculate the deviation δ_θ from a linear reduction with an average transmission ratio \bar{n} :

$$\delta_\theta = \mathcal{T}(\theta)/\bar{n} - \theta \quad (7)$$

Figure 10a shows, as an example, the measured deviation for the positive and negative contact cases with a total of 200 measurement points and an average reduction ratio of 1:1024. The visible peaks correspond to the 36 tooth pairings of the ring gear of the last reduction stage of the planetary gear. Figure 10b shows the backlash depending on the output angle. It is obtained as the difference between positive and negative contact $B = \bar{n}(\delta_{+\theta} - \delta_{-\theta})$. The Figure shows that the backlash varies between 40 and 250 degrees on the motor side and does indeed depend on the angle θ . The nonlinear transmission ratio stems from the mechanical manufacturing imperfections of the gears and is therefore slightly different for every gear.

2.4. Friction

A friction model, including static Coulomb and viscous friction, is sufficient to model the overall friction in the gear:

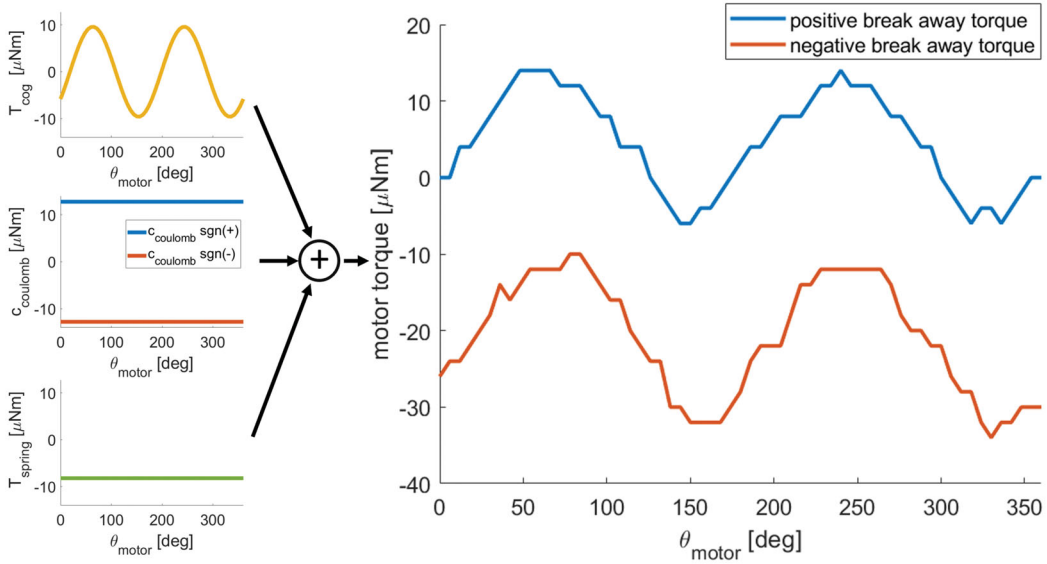


Figure 11. The Figure on the right shows the measured break away torque in positive and negative motor direction depending on the motor angle. The break away torque is a superposition of Coulomb friction, cogging torque and the resistance of the torsion spring.

$$F_{friction} = c_{coulomb} \text{sgn}(\dot{\theta}_{gear}) + c_{viscous} \dot{\theta}_{gear} \quad (8)$$

By commanding the positioner to a given motor position and then increasing the motor torque gradually till the rotor starts to move, we can measure the break-away torque at this motor position. If the motor is in gear contact, the break-away torque consists of the gear's Coulomb friction, the motor resistance torque F_{motor} and the torque from the play-reduction spring $T_{spring} = nk(\theta - \theta_{ref})$:

$$T_{ba} = F_{motor} + c_{coulomb} \text{sgn}(\dot{\theta}_{gear}) + T_{spring} \quad (9)$$

Note that the motor resistance torque F_{motor} includes the motor friction and also the magnetic reluctance (cogging) torque of the not powered motor. Since the friction $F_{friction}$ in the gear is much bigger than the one in the motor, we can neglect the friction in the motor, and therefore, simplify that the motor resistance torque consists only out of the cogging torque ($F_{motor} = T_{cog}$). Hence, F_{motor} is a conservative torque such that:

$$\int_0^{360} F_{motor} d\theta_{motor} = 0 \quad (10)$$

Figure 11 shows the measured positive and negative break-away torque for one full turn of the motor. The Figure shows that a higher torque is needed to turn the motor in the negative direction since it has to push against the torsion spring. Furthermore, both curves have a double sinusoid, which reveals a cogging torque T_{cog} with two favorable positions per motor turn. One full turn of the motor moves the output only slightly due to the reduction, and hence the torque of the spring here is assumed constant. The superposition of torsion spring, Coulomb friction, and cogging torque is apparent. By averaging the break-away torque over the full turn, we can calculate the Coulomb constant and the local torque of the spring:

$$T_{spring} = (\bar{T}_{+ba} + \bar{T}_{-ba})/2 \quad (11a)$$

$$c_{coulomb} = \bar{T}_{+ba} - \bar{T}_{spring} \quad (11b)$$

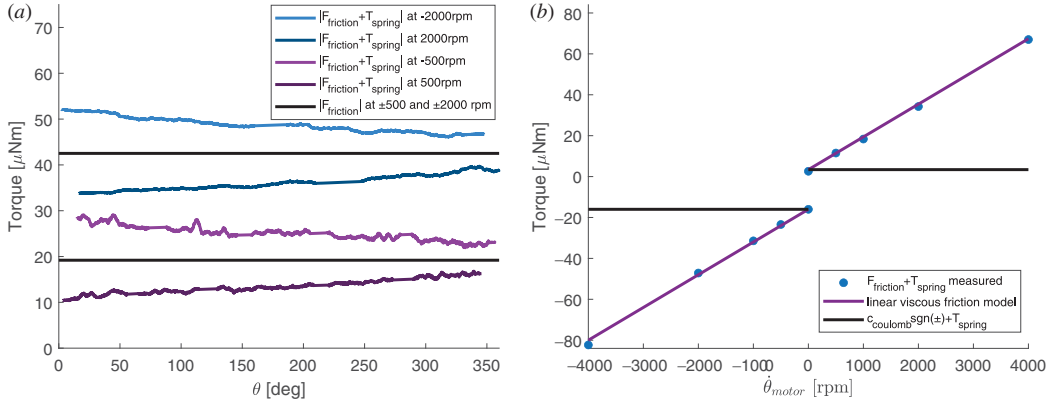


Figure 12. Left: torque required to move the motor at a constant speed of ± 500 and ± 2000 rpm depending on θ . Right: torque required to move the motor depending on θ .

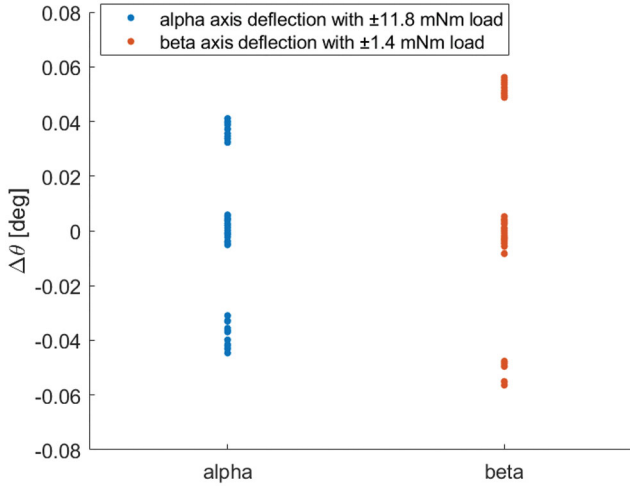


Figure 13. The Figure shows multiple measurements of applying a torque of ± 11.8 mNm on the alpha and ± 1.4 mNm on the beta axis.

Figure 12a shows the required torque to move the motor at constant speeds of ± 500 and ± 2000 rpm over the whole output workspace. It shows that depending on the direction, the motor drives against or with the torsion spring. The linear increase of the torsion spring is visible with the highest torque at $\theta = 0$. Figure 12b shows the linear relation between required torque and motor speed, confirming the viscous friction model.

2.5. Stiffness

The stiffness of the gear k is measured by charging the output of the axes with a negative and positive torque and measuring the angular deflection with the metrology camera. Figure 13 shows multiple measurements of applying a torque of ± 11.8 mNm on the alpha and ± 1.4 mNm on the beta axis, which results in a stiffness of $k = T_{\text{ext}}/\Delta\theta = 337$ mNm/deg for alpha and 25 mNm/deg for the beta axis.

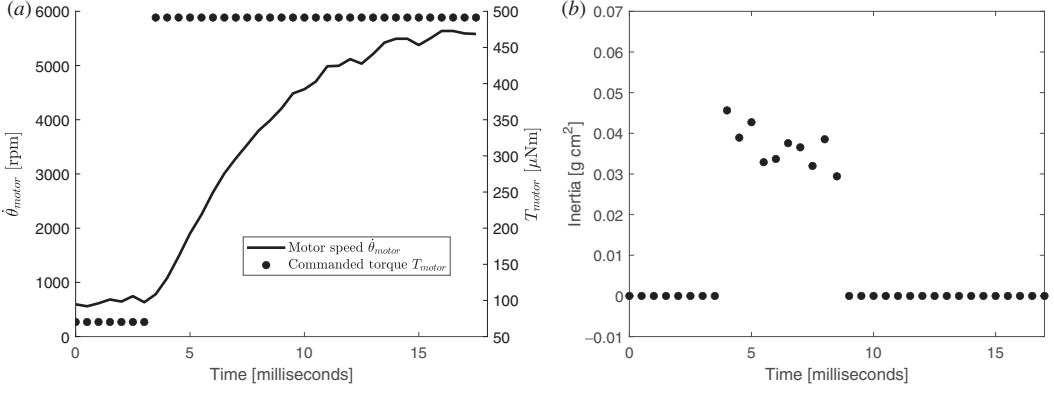


Figure 14. Left: the motor speed $\dot{\theta}_{motor}$ reacts to a sudden torque change, the motor accelerates in about 15 milliseconds from 600 to 5600 rpm. Right: from the motor acceleration and applied torque the inertia of the motor is estimated.

2.6. Moment of inertia

The total inertia $J = J_{motor} + J_{load}$ is obtained by integrating the force applied on the rotation axis over a certain time and dividing it by the velocity change:

$$J = \frac{\int_{t_1}^{t_2} (T_{motor} - F_{motor} - F_{friction} - T_{spring}) dt}{\dot{\theta}_{motor_{t_2}} - \dot{\theta}_{motor_{t_1}}} \quad (12)$$

Figure 14 shows how the rotor of the alpha motor accelerates due to a sudden torque change from 70 to 490 μNm . It takes only about 15 milliseconds to accelerate from 600 to 5600 rpm. The inertia of the motor is very small with 0.035 g cm^2 . Note that, the output inertia J_{load} is negligible compared to the rotor inertia J_{motor} due to the large reduction ratio of 1:1024.

3. Control

Motion planning algorithms calculate the exact path the robots have to follow such that they do not collide with each other and also make sure, that they end up at the correct assigned targets. From the pre-calculated trajectories $\mathbf{r}_{cmd}(t)$ the motor angles are obtained by:

$$\theta_{motor} = \mathcal{T}(\mathcal{P}^{-1}(\mathbf{r}_{cmd})) \quad (13)$$

3.1. Motor model

Three-phase brushless DC motors with a permanent magnet on the rotor drive each rotation axis (Figure 15). The alpha axis motor has a diameter of 12 mm, and the beta axis one has 6 mm, respectively. The magnet of the rotor naturally tries to align itself with the magnetic field generated by the coils. The motor windings are in Delta connection with the following electrical model for the three coils, whereas u is the voltage over the coil, R is the coil resistance, i is the electric current in the coil, and λ is the flux linkage of the coil.

$$\begin{pmatrix} u_{AB} \\ u_{BC} \\ u_{CA} \end{pmatrix} = \begin{pmatrix} R_{AB} & 0 & 0 \\ 0 & R_{BC} & 1 \\ 0 & 0 & R_{CA} \end{pmatrix} \underbrace{\begin{pmatrix} i_{AB} \\ i_{BC} \\ i_{CA} \end{pmatrix}}_{\mathbf{i}} + \frac{d\lambda}{dt} \quad (14)$$

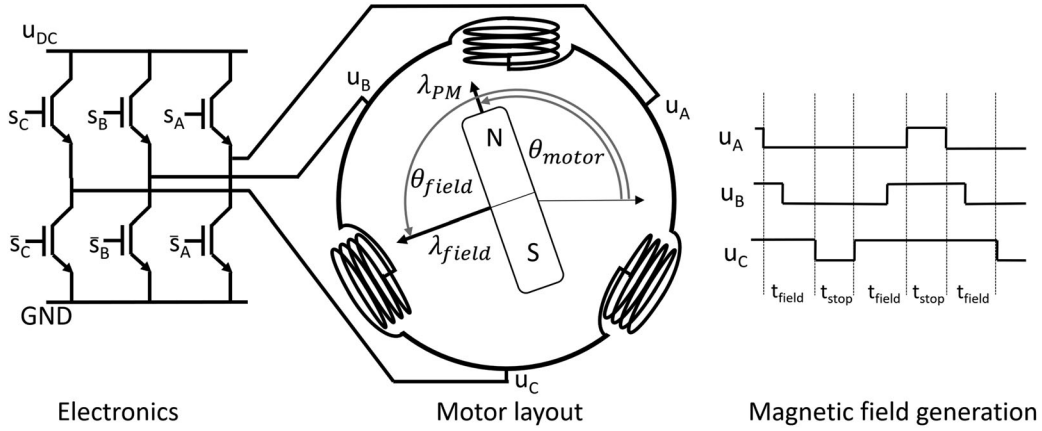


Figure 15. The figure shows the Delta configuration of the electric motor. Every phase is connected to an H bridge which can apply either zero or u_{dc} volts. Three synchronized PWM signals drive the three motor phases in order to generate a rotating magnetic field.

Here, we assume that the stator windings have a sinusoidally distributed magnetomotive force and that magnetic saturation is neglected. The vector λ represents the flux linkages of every coil:

$$\lambda = \mathbf{L}\mathbf{i} + \lambda_{PM} = \mathbf{L}\mathbf{i} + \lambda_{PM} \begin{pmatrix} \sin(\theta_{motor}) \\ \sin(\theta_{motor} + 120^\circ) \\ \sin(\theta_{motor} - 120^\circ) \end{pmatrix} \quad (15)$$

Whereas the matrix \mathbf{L} contains the self and mutual inductances. The coil inductances do not depend on the rotor position since the rotor consists mainly of the dipole magnet with a reluctance similar to air, which means that the activated coils do not induce a reluctance torque. λ_{PM} is the sinusoidal flux linkage of the permanent magnet. The torque is obtained with the co-energy method,^[38] with the number of poles equal two:

$$T_{motor} = \frac{\partial}{\partial \theta_{motor}} \left(\frac{1}{2} \mathbf{i}^T \mathbf{L} \mathbf{i} + \mathbf{i}^T \lambda_{PM} \right) + T_{cog} \quad (16)$$

These small motors with ironless windings have a very low inductance compared to the mechanical time constant. Therefore, we can simplify Equation 14 and assume an instantaneous current for a given applied voltage over a coil:

$$i_{AB} = \frac{u_{AB} - \lambda_{PM} \dot{\theta}_{motor} \cos(\theta_{motor})}{R_{AB}} \quad (17)$$

A pulse width modulation (PWM) controls the voltage applied to every phase. The three PWM signals are timed, such that a directional magnetic field is created. Figure 15 shows the correct symmetric timing of the PWM signals. The waiting time t_{stop} controls the average intensity of the generated magnetic field λ_{field} and the relative duty cycle differences during t_{field} control the correct field angle θ_{field} . The duty cycle of the PWM signal is proportional to the average applied voltage on one phase and can range between a tension of zero and u_{dc} . A directional magnetic field is created with duty cycles such that the average voltages correspond to:

$$u_A = 0.5 \cdot u_{cmd} \cdot (1 + \cos(\theta_{field} + 120^\circ)) \quad (18a)$$

$$u_B = 0.5 \cdot u_{cmd} \cdot (1 + \cos(\theta_{field} - 120^\circ)) \quad (18b)$$

$$u_C = 0.5 \cdot u_{cmd} \cdot (1 + \cos(\theta_{field})) \quad (18c)$$

Whereas u_{cmd} controls the intensity and must lie between $0 \leq u_{cmd} \leq u_{dc}$. The voltage applied to one coil is, therefore, e.g. $u_{AB} = u_B - u_A$. We can finally calculate the applied mechanical torque depending on u_{cmd} , θ_{field} and θ_{motor} by inserting Equations 17 and 18 into 16 and further simplifying that $R_{ab} = R_{bc} = R_{ca} = R$:

$$T_{motor} = \underbrace{\frac{3p_n \lambda_{PM} \sqrt{3}}{4R} \frac{1}{2} u_{cmd} \sin(\theta_{field} - \theta_{motor})}_{T'_{motor}} - \underbrace{\frac{3p_n \lambda_{PM}}{4R} \lambda_{PM} \dot{\theta}_{motor}}_{F_{BEMF}} + T_{cog} \quad (19)$$

The torque can be divided into three parts. The first T'_{motor} depends on u_{cmd} and also the difference between θ_{field} and θ_{motor} . This torque tries to align the magnet with the generated magnetic field since it is maximum for $|\theta_{field} - \theta_{motor}| = 90$ and is zero for $\theta_{field} = \theta_{motor}$. The second part is due to the back electromotive force (BEMF), which depends on the motor speed and behaves like a viscous friction torque. The last one is the cogging torque which has already been introduced.

3.2. Controller

In order to cover the whole workspace of 360 degrees at the output, the motor has to perform 1024 full turns. The absolute position is retained in the microcontroller with a counter, which increases or decreases when the motor performs a full turn. The motors are either commanded in an open or closed-loop control. In open-loop control, the motors are driven with a high voltage u_{cmd} such that the magnet of the rotor follows the magnetic field vector closely. We can assume that $\theta_{field} \approx \theta_{motor}$, since the inertia seen by the motor is relatively small. The advantage of the open-loop control is that no sensor is needed. The disadvantages are that much energy is lost to heat and that the motor can slip a turn without noticing. This happens when the motor torque is not strong enough and the rotor does not manage to follow the rotating magnetic field resulting in a wrong motor turn count.

The energy efficiency increases with the angular offset between θ_{field} and θ_{motor} and reaches its maximum at 90 degrees. The closed-loop control maintains this 90 degrees angular difference by using hall sensors. The intensity of the torque is controlled by adjusting u_{cmd} and its sense of rotation by setting the commanded field difference to ± 90 degrees of the rotor position:

$$u_{cmd} \propto T'_{motor} \quad (20a)$$

$$\theta_{field} = \theta_{motor} + \text{sgn}(T_{motor}) \cdot 90^\circ \quad (20b)$$

We can implement a closed-loop PI controller acting on u_{cmd} , since u_{cmd} is proportional to T'_{motor} . The BEMF and cogging torque is compensated with a feedforward command. Other feedforward compensations include the friction torque $F_{friction}$, play reduction spring T_{spring} and inertia J :

$$T'_{motor} = K_P(\theta_{motor}^{cmd} - \theta_{motor}^{est}) + K_I \int_0^t (\theta_{motor}^{cmd} - \theta_{motor}^{est}) d\tau \quad \text{feedback} \quad (21a)$$

$$+ \underbrace{T_{cog} + F_{BEMF} + F_{friction} + T_{spring} + J\ddot{\theta}_{motor}^{cmd}}_{T'_{ba}(\theta_{motor}^{cmd}) + c_{tot}\dot{\theta}_{motor}^{cmd} + J\ddot{\theta}_{motor}^{cmd}} \quad \text{feedforward} \quad (21b)$$

Note that the feedforward compensation terms all rely on the commanded position, speed, and acceleration generated by the path planning. Therefore, no noisy derivated sensor measurements are used. The position dependent term is the break-away torque T_{ba} as introduced above. The second term c_{tot} consists of the viscous friction and BEMF and depends linearly on the

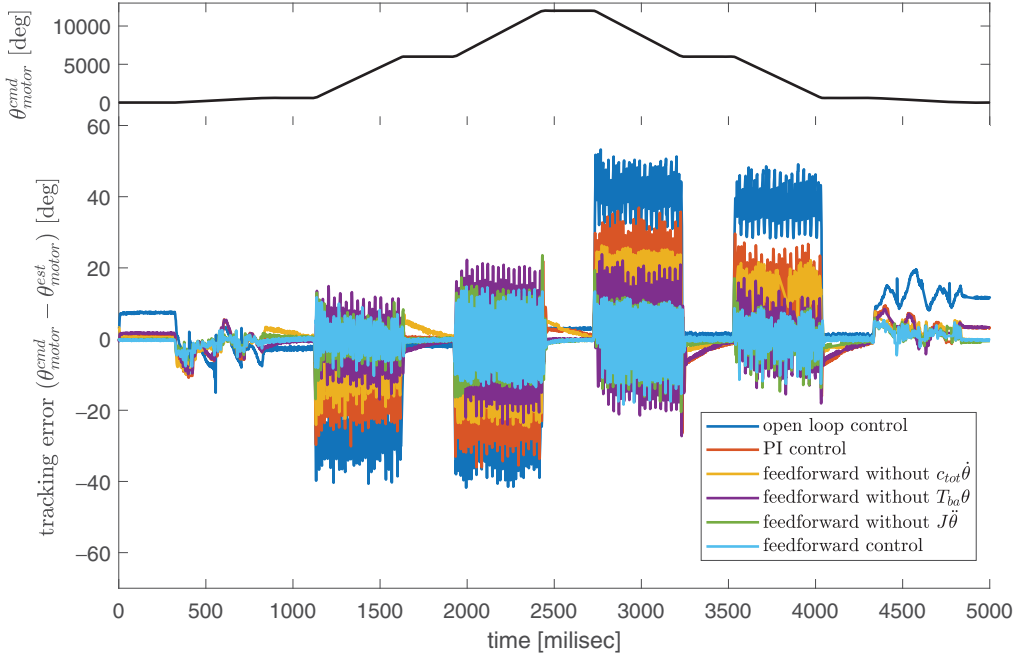


Figure 16. The upper part shows the commanded path for the beta motor. It consist of three ramps with constant speeds (200, 1800, and 2000 rpm) in positive and negative direction. The lower image shows the error between commanded and measured position for different implemented controllers following the path.

motor velocity. Finally, the last term is the compensation of the total inertia J . Limits in the path planning algorithm make sure that the maximum acceleration and speed are within the specified boundaries. The feedback term generated by the PI controller only depends on the difference of the commanded position and the measured position by the hall sensors. The PI terms correct only the model uncertainties since the feedforward term contains the positioner model. **Figure 16** shows the controller performance of the beta motor as a performance example. The upper part of the figure shows the commanded path, which consists of three ramps with constant speeds (200, 1800, and 2000 rpm) first in positive and then in negative direction. The lower image shows the error between commanded and measured positions for different implemented controllers which followed the path. The worst performance is obtained with the open loop controller with a tracking error up to 55 degrees. With the feedforward control, the tracking error can be lowered down to 15 degrees. The figure shows also how the feedforward control performance decreases when either the linear speed, break-away, or inertia compensation is omitted.

With the feedforward control, we can also detect possible collisions between adjacent positioners or malfunctions. When a collision happens, the external torque T_{ext} raises, which the PI controller tries to counteract. Therefore whenever unmodelled perturbations make the feedback term raise over a certain threshold, a collision is detected, and the positioner stopped. With a sampling frequency of 2000 Hz, a collision can be detected in just a few milliseconds. The collision detection condition is given when:

$$\left| K_P(\theta_{motor}^{cmd} - \theta_{motor}^{est}) + K_I \int_0^t (\theta_{motor}^{cmd} - \theta_{motor}^{est}) d\tau \right| > T_{threshold} \quad (22)$$

The threshold $T_{threshold}$ corresponds to the additional torque the controller has to provide to overcome all unmodelled perturbations. This threshold should be chosen such that no false collisions are detected due to uncertainties in the model parameters. For this we can examine the

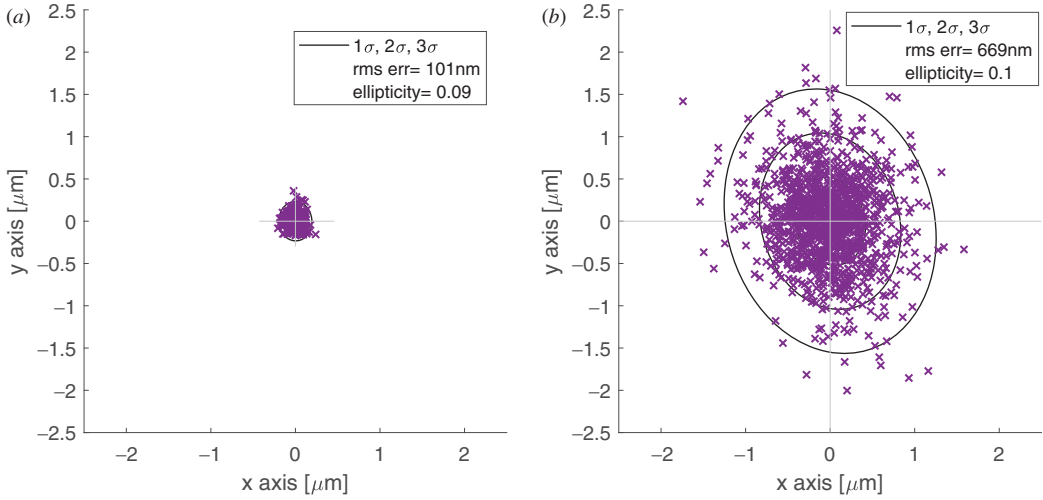


Figure 17. Three targets spaced by 1 μm are sequentially approached. Every target is revisited 300 times. Left: for the alpha axis one micrometer difference between the targets corresponds to 7.7 degrees at the motor with a lever of 7.6 mm (folded configuration) Right: for the beta axis one micrometer difference between the targets corresponds to 3.9 degrees at the motor with an arm length of 15 mm.

maximum angular tracking error $\Delta\theta = \theta_{motor}^{cmd} - \theta_{motor}^{est}$ at which the torque threshold detects a collision. The angular error range in which a collision is detected depends on the anti windup term $T_{I-max} = K_I \int \Delta\theta d\tau$ of the integrator:

$$\Delta\theta_{coll-min} = (T_{threshold} - T_{I-max})/K_I \quad (23a)$$

$$\Delta\theta_{coll-max} = (T_{threshold} + T_{I-max})/K_I \quad (23b)$$

Irrespective of the actual value of the integrator term, a collision is detected when the tracking error $\Delta\theta$ is between $\Delta\theta_{coll-min}$ and $\Delta\theta_{coll-max}$. Figure 16 shows that the closed loop controller keeps the motor tracking error to within 20 degrees for any commanded speed and acceleration. The torque threshold and the anti-windup can now be derived by choosing $\Delta\theta_{coll-min}$ to be higher than the 20 degrees error with a certain margin. This guarantees that no false collision detection occurs. For example with a $\Delta\theta_{coll-min}$ of 120 degrees and a motor speed of 2000 rpm the maximum time till a collision is detected is 16 milliseconds, if we neglect the anti-windup term.

3.3. Positioning precision

The stringent positioning requirements must be met during the target observation when the positioner is at a standstill. In order to guarantee high standstill precision, the approach trajectory of θ_{motor} to the target is crucial. A negative approach to the target assures excellent repeatability since the motor moves against the torsion spring and closes, therefore, all backlash in the gear.

By placing the calibration camera close to the positioner and zooming in to the back-illuminated fiber, we can significantly increase the position measurement precision of the camera (Figures 3 and 17) in order to assess the placement precision of the two axes. Figure 18 shows approach moves to three different targets separated by 1 μm for the alpha and beta axis. For every axis, the motor is commanded to the three positions sequentially. After each move, the camera takes an image to verify the position. Every position is revisited 300 times. For the alpha axis, the one micrometer difference between the targets corresponds to 7.7 degrees at the motor or 0.0075 degrees at the output with a lever of $15-7.4=7.6$ mm, since the positioner was in a

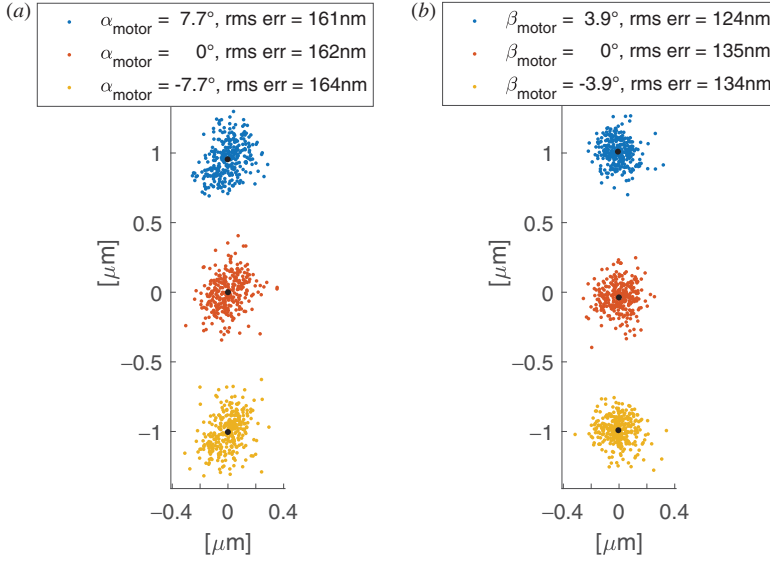


Figure 18. Two measurement setups of the camera (Figure 3) are used. The first has the camera placed very close to the positioner such that only a small fraction of the robot's workspace is visible. In addition, several images are averaged before the centroid is calculated. This leads to good measurement repeatability of 101 nm RMS shown on the left. This set up has been used to create Figure 17. The Figure on the right shows the measurement repeatability of a static fiber with the camera placed such that the whole workspace is visible with an RMS repeatability of 669 nm. All other measurements have been obtained with this second set up.

folded position for the measurements. One micrometer position difference corresponds to 3.9 degrees for the beta motor or 0.0038 degrees at the gear output with a lever of 15 mm. Note that the angular difference is smaller than the calibrated backlash, and therefore the positioner performs a back and forth movement of 840 degrees at the motor to go from one target to the next. This makes sure that the approach move is bigger than the backlash and therefore the backlash gap is fully closed. The Figure shows that the rms repeatability for both axes is below 170 nanometers and that targets separated by 1 μm can well be distinguished.

The measurements are taken in a temperature-controlled room with minimized airflow. Figure 17a shows the measurement repeatability of a static fiber with the same camera set up. It shows that a significant fraction of the error comes from the metrology system. The rms repeatability of a static fiber is 101 nm compared to about 160 nm for the alpha and 130 nm for the beta placement.

4. Camera feedback

In order to reach a target galaxy or star $\mathbf{r}_{\text{target}}$, the motors are commanded to the correct angular position according to (where $\mathbf{r}_{\text{cmd}_i} = \mathbf{r}_{\text{target}}$):

$$\theta_{\text{motor}_i}^{\text{cmd}} = \mathcal{T}(\mathcal{P}^{-1}(\mathbf{r}_{\text{cmd}_i})) \quad (24)$$

The absolute position accuracy depends mainly on the exactness of the calibrated positioner parameters, such as arm lengths and non-constant reduction ratio. As well as how closely the introduced model describes the behavior of the positioner. Some telescopes require a good absolute position accuracy since they do not have a metrology system that verifies the correct fiber placement before observations. Other telescopes have a dedicated metrology system which consists of one or several cameras observing the focal plane and which can determine accurately the x, y location of the fiber end. In this section, we show how the metrology system can be used to further decrease the positioning errors of the robots iteratively and how the model parameters can be calibrated in the focal plane.

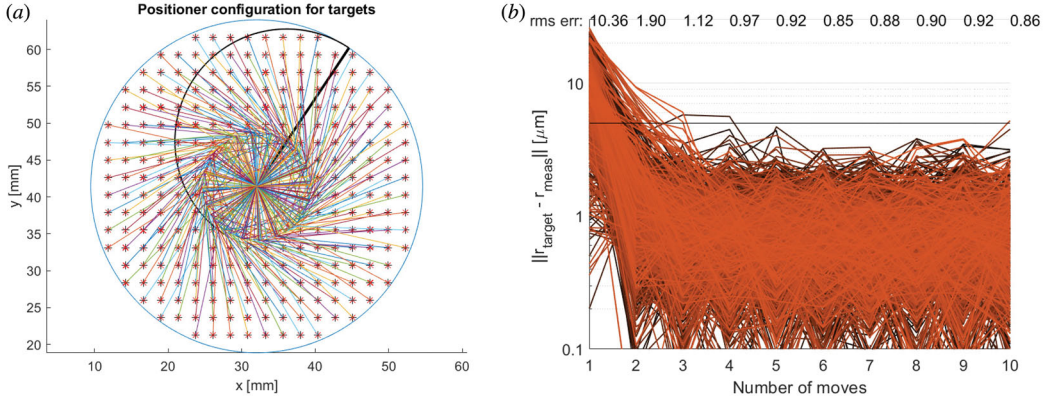


Figure 19. Left: the figure shows the workspace of one positioner and the arm configurations needed to reach a set of targets. The targets are distributed over the whole workspace. Every target is approached first without any camera feedback (blind move) with terminal motor angles obtained by Equation 24. After the blind move, nine camera correction moves were executed with updated commanded target positions according to Equation 25. This procedure was repeated five times for every target. Right: the figure shows the error between target and measured positions for every move. Move one represents the blind move with an RMS positioning error of 10.36 μm . After only two camera corrections (move three) the RMS positioning error is decreased to 1.12 μm . Note that for every move the final approach to the target is against the torsion spring to close all backlash in the gear.

4.1. Precision iterations

For precision iterations, the positioner first drives to a target without feedback from the camera system (called blind move). Then the fiber gets back-illuminated and the camera takes a picture to determine its position. With the error between the measured and commanded position, the commanded position is updated according to Equation 25, and a small correction maneuver is executed with updated motor commands (Equation 24). This procedure is repeated until the required precision is reached.

$$\Delta \mathbf{r}_i = \mathbf{r}_{\text{cmd}_i} - \mathbf{r}_{\text{meas}_i} \quad (25a)$$

$$\mathbf{r}_{\text{cmd}_{i+1}} = \mathbf{r}_{\text{cmd}_i} + \Delta \mathbf{r}_i \quad \text{for } i > 1 \quad (25b)$$

Figure 19a shows a set of 244 targets distributed over the whole workspace and its corresponding arm configurations. Every shown target was approached 5 times, plus nine correction moves per approach. Figure 19b shows the corresponding measured RMS positioning errors for every move. It shows that the first/blind move has a measured positioning error of 10.36 μm RMS over all targets. The positioning error decreases until it settles around 0.9 μm RMS. The repeatability of the positioner and the measurement repeatability of the camera limit further improvement. The most significant limiting part here is the camera repeatability, which is shown in Figure 17b with 669 nm RMS.

4.2. In focal plane calibration

Once the positioners are installed in the focal plane, the metrology system can calibrate the exact location $\mathbf{r}_{\text{center}}$ and orientation α_{off} of every positioner. The positioners are densely populated and cannot freely move without risking a collision with their neighbors. Therefore, correct path planning ensures that there is a larger safety zone around the moving arms during calibration. Every positioner is driven to different arm configurations with axis angles θ_i . A least-squares optimization minimizes then the difference between measured $\mathbf{r}_{\text{meas}_i}$ and modelled fiber positions $\mathbf{r}_{\text{target}_i}$ in order to find the parameters l_a , l_b , $\mathbf{r}_{\text{center}}$, and α_{off} .

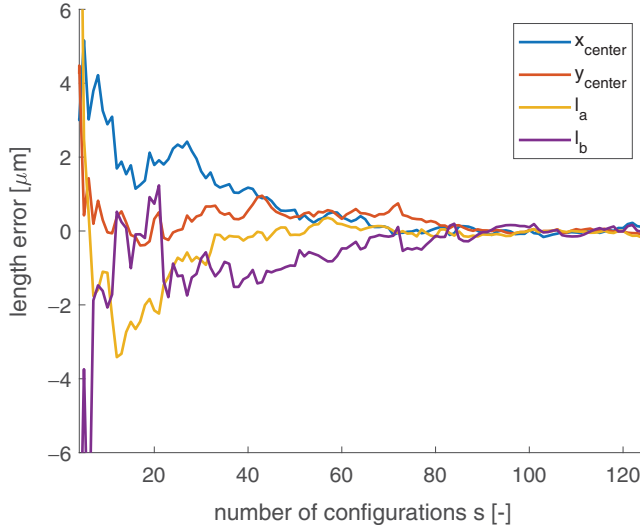


Figure 20. The figure shows the estimation error of the positioner center and arm lengths depending on how many different configurations spread across the workspace are included in the optimization algorithm.

$$\min_{\mathbf{r}_{center}, l_a, l_b, \alpha_{off}} \sum_{i=1}^s (\mathbf{r}_{meas_i} - \mathbf{r}_{target_i})^2 \quad (26)$$

Figure 20 shows how the parameters converge depending on the number s of measured configurations. The optimization algorithm needs about 80 different configurations spread across the whole workspace until the estimated positioner center and arm lengths are well below one micrometer.

4.3. Adaptive calibration

Without recalibration, the blind move precision decreases if the calibrated parameters change over the lifetime of the telescope. A telescope with a metrology system such as SDSS-V and DESI can correct these blind move positioning degradations with the expense of a few more correction iterations. We performed lifetime tests to examine how parameters change due to wear. A lifetime test consists of repeated measurement cycles. Each cycle starts with an automatic calibration followed by approaching a set of random targets distributed in the workspace, such as shown in Figure 19a. The lifetime test allows us to simulate telescope operation and, also, monitor the change of parameters due to the repeated calibrations. Each cycle consists of a total of 15260 positioner moves and takes about 7 hours of continuous operation. Figure 21 shows how the calibrated arm lengths change for two measured robots over the performed cycles. The Figure shows that the arm length variations do not change much due to wear and stay within about one micrometer. Figure 22 shows the evolution of the non-linear transmission value δ_0 of the beta axis for the same two robots. The non-linear transmission can locally change up to 0.15 degrees, which corresponds to a positioning error increase up to several tenths of micrometers. This degradation of the blind move precision leads to an increase in the number of correction moves needed to reach the required accuracy. Generally, the number of correction moves should be kept low due to the limited available time between observations. Here we propose, an adaptive calibration method for the nonlinear transmission, which allows keeping the blind move precision low without the need for specific recalibration measurements. Furthermore, it allows us to monitor the health of a positioner if e.g. a tooth of the reduction gear breaks. The method

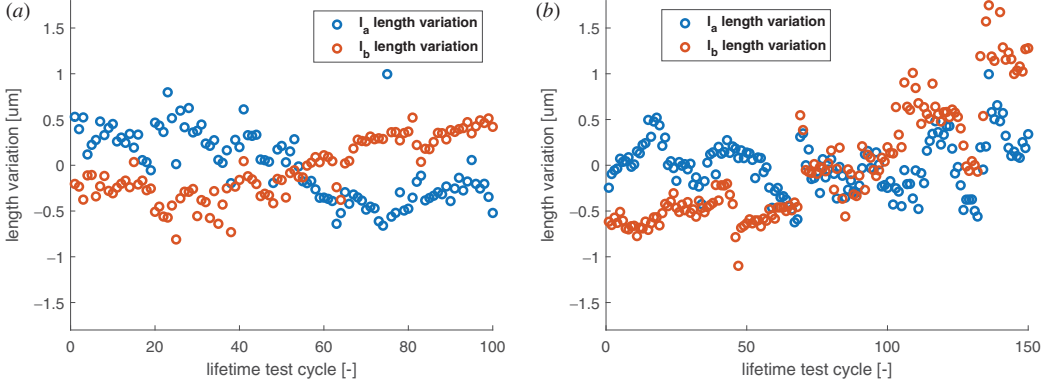


Figure 21. Temporal change in arm's lengths for two fiber positioners.

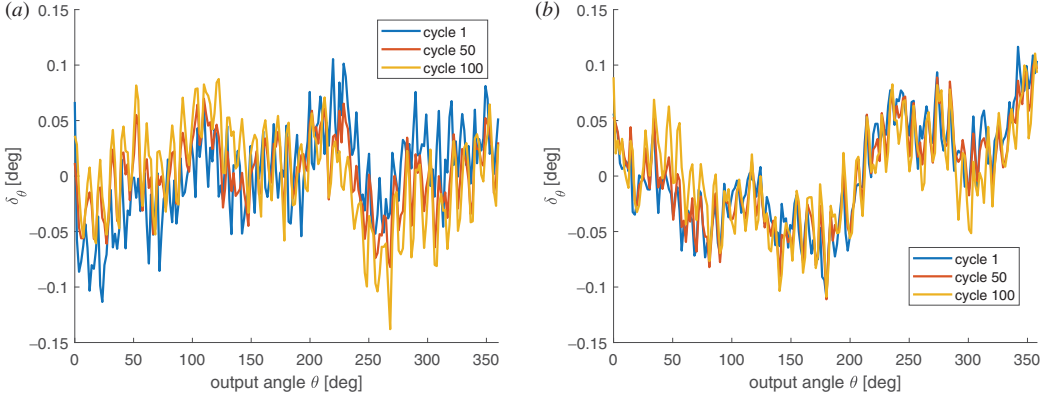


Figure 22. The figure shows the evolution of the non-linear transmission value δ_θ of the beta axis for two robots. The measured non-linear transmission of cycle 1, 50, and 100 is shown.

uses the information of the measured fiber positions during normal operation in order to update the model of the non-linear transmission model.

A bivariate Gaussian distribution describes the probability to obtain a fiber position \mathbf{z} given the real position \mathbf{r} with covariance matrix $\Sigma_{\mathbf{r}}$:

$$p(\mathbf{z}|\mathbf{r}) = \frac{1}{2\pi|\Sigma_{\mathbf{r}}|^{0.5}} \exp\left(-\frac{1}{2}(\mathbf{z} - \mathbf{r})^T \Sigma_{\mathbf{r}}^{-1}(\mathbf{z} - \mathbf{r})\right) \quad (27)$$

In order to estimate the most probable fiber position after an approach move, we first define two Gaussian distributions, one for the camera measurement and another one for the positioner accuracy (Figure 23). Given the measurement uncertainties of the camera described by the covariance Σ_{meas} and the real fiber position \mathbf{r} , the probability distribution of the measured fiber position \mathbf{r}_{meas} is $p(\mathbf{r}_{meas}|\mathbf{r})$. The measurement uncertainty of the camera x and y -axis is assumed independent:

$$\Sigma_{meas} = \begin{pmatrix} \sigma_x^2 & 0 \\ 0 & \sigma_y^2 \end{pmatrix} \quad (28)$$

Similarly, we define the probability of reaching \mathbf{r}_{cmd} given the true end position \mathbf{r} by $p(\mathbf{r}_{cmd}|\mathbf{r})$. The covariance matrix Σ_{cmd} of this distribution includes the uncertainty of the arm length and

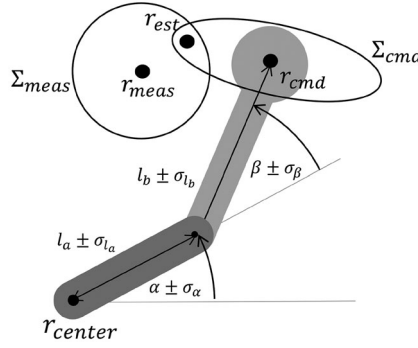


Figure 23. The figure shows the uncertainty ellipses of the measured and commanded fiber position.

the uncertainty of the motor output angles. The length and angle uncertainties of both axes are summed:

$$\begin{aligned} \Sigma_{cmd} &= \Sigma_{\alpha} + \Sigma_{\beta} \\ &= \mathbf{R}(\alpha_{cmd}) \begin{pmatrix} \sigma_{l_a}^2 & 0 \\ 0 & \sigma_{\alpha}^2 \end{pmatrix} \mathbf{R}^T(\alpha_{cmd}) + \mathbf{R}(\alpha_{cmd} + \beta_{cmd}) \begin{pmatrix} \sigma_{l_b}^2 & 0 \\ 0 & \sigma_{\beta}^2 \end{pmatrix} \mathbf{R}^T(\alpha_{cmd} + \beta_{cmd}) \end{aligned} \quad (29)$$

Whereas $\mathbf{R}(\alpha_{cmd})$ and $\mathbf{R}(\beta_{cmd})$ are the direction cosine rotation matrices transforming the uncertainty in length and angle to the x, y reference frame of the camera. **Figure 23** shows the commanded and measured fiber position with the corresponding covariance ellipsoids.

Multiplying both Gaussian distributions and scaling them with a factor c gives the likelihood of the fiber position \mathbf{r}_{est} given \mathbf{r}_{cmd} and \mathbf{r}_{meas} :

$$\mathcal{L}(\mathbf{r}_{est} = \mathbf{r}; \mathbf{r}_{cmd}, \mathbf{r}_{meas}) = p(\mathbf{r}_{cmd}, \mathbf{r}_{meas} | \mathbf{r}) = c \cdot p(\mathbf{r}_{cmd} | \mathbf{r}) \cdot p(\mathbf{r}_{meas} | \mathbf{r}) \quad (30)$$

The result is a new Gaussian distribution with mean \mathbf{r}_{est} , representing the most probable position of the fiber:

$$\mathbf{r}_{est} = \Sigma_{meas}(\Sigma_{meas} + \Sigma_{cmd})^{-1} \mathbf{r}_{cmd} + \Sigma_{cmd}(\Sigma_{meas} + \Sigma_{cmd})^{-1} \mathbf{r}_{meas} \quad (31)$$

With the inverse kinematics, we calculate the actual output angles of the positioner:

$$\theta_{est} = \mathcal{P}^{-1}(\mathbf{r}_{est}) \quad (32)$$

Finally, we can update the non-linear transmission vector $\tilde{\theta}_s$ according to:

$$\tilde{\theta}_{s_{new}} = \tilde{\theta}_s + (\theta_{est} - \theta_{cmd}) \text{ with } \min_s (\theta_{motor_{cmd}} - \tilde{\theta}_{motor_s}) \quad (33)$$

Note that for a positioner move with the motor command $\theta_{motor_{cmd}}$, only the parameter $\tilde{\theta}_s$ with the closest motor angle $\tilde{\theta}_{motor_s}$ is updated to $\tilde{\theta}_{s_{new}}$. The other parameters are not updated. The dashed line in **Figure 24** shows the updated non-linear transmission. For subsequent approach moves the updated transmission calibration is used:

$$\theta_{motor_{cmd}} = \mathcal{T}(\theta_{cmd} | \tilde{\theta}_{motor}, \tilde{\theta}_{new}) \quad (34)$$

With the results from the lifetime test, we can verify how well the adaptive calibration works. **Figure 25** shows the deviation δ_{θ} from a linear reduction for the test cycles 10 and 100, that have been obtained by repeated calibrations. It also shows the deviation obtained from the adaptive algorithm for the same cycles. The adaptive algorithm starts with the calibrated transmission at cycle one and uses the positioner moves for all subsequent cycles to update the calibration values. It shows that the adaptive algorithm manages to adequately track the change of the non-linear transmission.

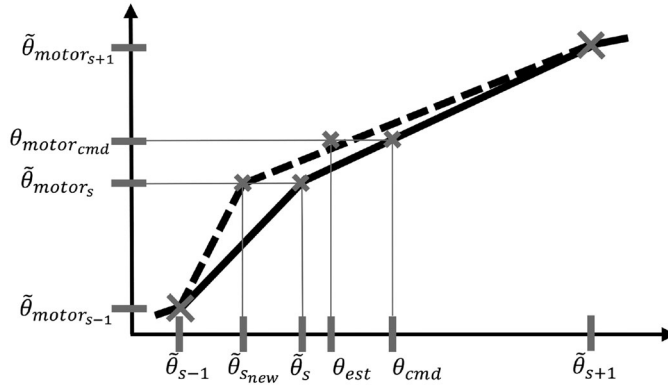


Figure 24. Update of non-linear transmission vector.

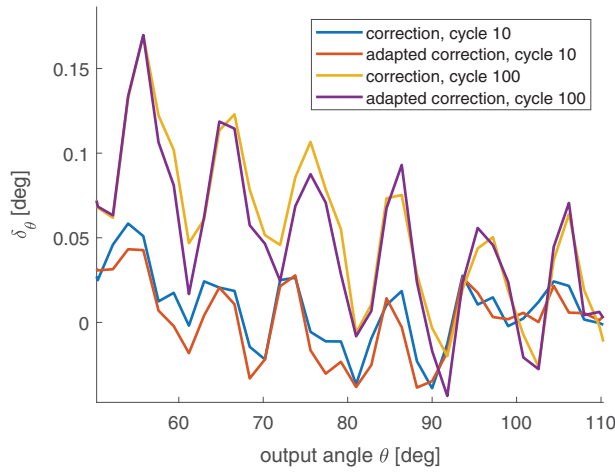


Figure 25. The figure shows the deviation δ_θ from a linear reduction once obtained by direct measurement and once obtained by the adaptive algorithm for the test cycles 10 and 100. It shows good tracking of the non-linear transmission by the adaptive algorithm.

Figure 26 shows the evolution of the first move error for the two positioners. The blue line shows the error for a positioner model with a simple linear reduction ratio. For red, the non-linear reduction ratio is calibrated just in the first cycle and then fixed for the whole lifetime test. Yellow shows the first move error obtained with the adaptive correction and purple with a recalibration for every cycle.

The efficiency of the adaptive calibration is well shown as it only performs slightly worse than when an up-to-date calibration is used. The Figure also shows the need for taking into account the non-linear transmission. It reduces the first move error by a factor of 3.5 compared to a model with a linear transmission.

5. Conclusion

We presented the design aspects of SCARA-like optical fiber positioners for Multi-Object Spectrographs. First, we studied a detailed mechanical model describing the correct behavior of the positioner. The model includes aspects such as nonlinear transmission, backlash, and friction. Measurement results are presented which validate the model.

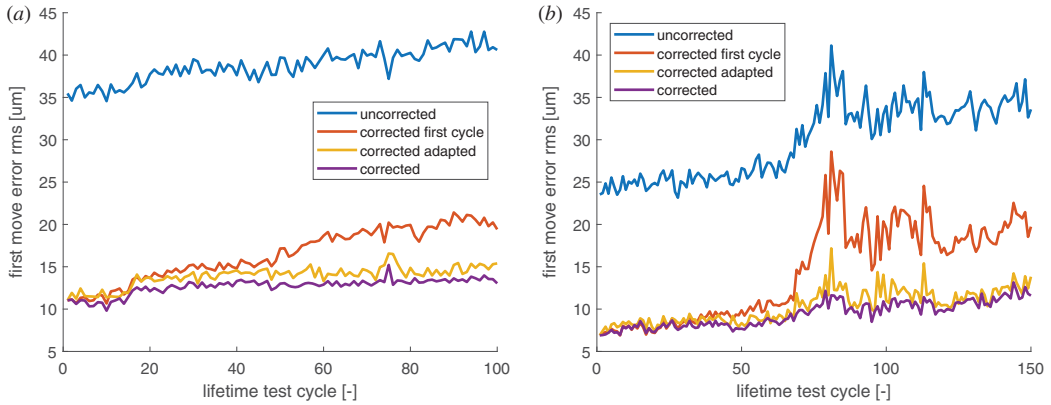


Figure 26. Evolution of the first move error for two positioners.

Based on the identified mechanical model, a motor control strategy is derived. In comparison to the DESI positioner, which uses an open loop control, the proposed feedforward closed loop controller has the advantage of reducing the dissipated heat and ensures that absolute accuracy can not be lost due to motor slippage. The model-based controller allows one to also detect collisions between neighboring positioners, which is an important feature due to overlapping workspaces of the units. The detection threshold of the method can be chosen so that false collision detections due to model uncertainties can be excluded. The only other alpha-beta positioner equipped with a collision detection system is the MOONS positioner which is based on applying a unique voltage to positioners and measuring the current when they touch. Our method has the advantage that the positioners do not have to be voltage isolated.^[16]

We propose a method, how the positioners can efficiently be commanded during normal operation of the telescope. By moving against the torsion spring, we propose a backlash closing target approach which guarantees a repeatability below one micrometer RMS (Figures 10 and 18). We show how the metrology camera of a telescope can be used to initialize the positioners after installation in the focal plane and how to decrease positioning errors iteratively. The method updates the calibrated positioner parameters during the regular operation of the telescope. This methodology ensures a continuously optimized performance of the positioners over the telescope's lifetime. The blind move error is reduced by a factor of 3.5 compared to a model without correction of the non-linear reduction gear. Furthermore, the method allows also to supervise the health status of the positioners.

Acknowledgments

The authors would like to thank the workshops ATME and ATPR from EPFL for the production of the prototypes.

Disclosure statement

No potential conflict of interest was reported by the author(s).

Funding

This project was supported by the SNF/FLARE grants (MOONS-1: 20FL21-166919, SDSS-V: 20FL21-185771 and DESI: 20FL21-160476) and through contribution from the ARC/SDSS-V funding.

ORCID

Luzius Kronig  <http://orcid.org/0000-0002-8894-6591>

References

- [1] Smee, S.A.; Gunn, J.E.; Uomoto, A.; Roe, N.; Schlegel, D.; Rockosi, C.M.; Carr, M.A.; Leger, F.; Dawson, K.S.; Olmstead, M.D.; Brinkmann, J.; Owen, R.; Barkhouser, R.; Honscheid, K.; Harding, P.; Long, D.; Lupton, R.; Loomis, C.; Anderson, L.; Annis, J.; Bernardi, M.; Bhardwaj, V.; Bizyaev, D.; Bolton, A.; Brewington, H.; Briggs, J.; Burles, S.; Burns, J.; Castander, F.; Connolly, A.; Davenport, J.; Ebelke, G.; Epps, H.; Feldman, P.; Friedman, S.; Frieman, J.; Heckman, T.; Hull, C.; Knapp, G.; Lawrence, D.; Loveday, J.; Mannery, E.; Malanushenko, E.; Malanushenko, V.; Merrelli, A.; Muna, D.; Newman, P.; Nichol, R.; Oravetz, D.; Pan, K.; Pope, A.; Ricketts, P.; Shelden, A.; Sandford, D.; Siegmund, W.; Simmons, A.; Smith, D.; Snedden, S.; Schneider, D.; SubbaRao, M.; Tremonti, C.; Waddell, P.; York, D. The multi-object, fiber-fed spectrographs for the Sloan digital sky survey and the Baryon oscillation spectroscopic survey. *AJ*. **2013**, *146*, 32.
- [2] Dong, X.Y.; Wu, X.-B.; Ai, Y.L.; Yang, J.Y.; Yang, Q.; Wang, F.; Zhang, Y.X.; Luo, A.L.; Xu, H.; Yuan, H.L.; Zhang, J.N.; Wang, M.X.; Wang, L.L.; Li, Y.B.; Zuo, F.; Hou, W.; Guo, Y.X.; Kong, X.; Chen, X.Y.; Wu, Y.; Yang, H.F.; Yang, M. The large sky area multi-object fibre spectroscopic telescope (LAMOST) Quasar survey: Quasar properties from data release two and three. *AJ*. **2018**, *155*, 189.
- [3] Gil de Paz, A.; Gallego, J.; Carrasco, E.; Iglesias-Paramo, J.; Cedazo, R.; Vilchez, J.; Garcia-Vargas, M.; Arrillaga, X.; Carrera, M.; Castillo-Morales, A.; Castillo-Dominguez, E.; Eliche-Moral, M.; Ferrusca, D.; Gonzalez-Guardia, E.; Lefort, B.; Maldonado, M.; Marino, R.; Martinez-Delgado, I.; Morales, I.; Mujica, E.; Paez, G.; Pascual, S.; Perez-Calpena, A.; Sanchez-Penim, A.; Sanchez-Blanco, E.; Tulloch, S.; Velazquez, M.; Zamorano, J.; Aguerri, A.; Barrado, D.; Bertone, E.; Cardiel, N.; Cava, A.; Cenarro, J.; Chavez, M.; Garcia, M.; Guichard, J.; Guzman, R.; Herrero, A.; Huelamo, N.; Hughes, D.; Jimenez-Vicente, J.; Kehrig, C.; Marquez, I.; Masegosa, J.; Mayya, Y.; Mendez-Abreu, J.; Molla, M.; Munoz-Tunon, C.; Peimbert, M.; Perez-Gonzalez, P.; Perez-Montero, E.; Rodriguez, M.; Rodriguez-Espinoza, J.; Rodriguez-Merino, L.; Rosa-Gonzalez, D.; Sanchez-Almeida, J.; Sanchez-Contreras, C.; Sanchez-Blazquez, P.; Sanchez-Moreno, F.; Sanchez, S.; Sarajedini, A.; Serena, F.; Silich, S.; Simon-Diaz, S.; Tenorio-Tagle, G.; Terlevich, E.; Terlevich, R.; Torres-Peimbert, S.; Trujillo, I.; Tsamis, Y.; Vega, O.; Villar, V. Megara: A new generation optical spectrograph for GTC. *Proc. SPIE*. **2014**, *9147*, 9147–9147.
- [4] Cunha, E.D.; Hopkins, A.M.; Colless, M.; Taylor, E.; Blake, C.; Howlett, C.; Magoulas, C.; Lucey, J.; Lagos, C.; Kuehn, K.; Gordon, Y.; Barat, D.; Bian, F.; Wolf, C.; Cowley, M.; White, M.; Achitouv, I.; Bilicki, M.; Bland-Hawthorn, J.; Bolejko, K.; Brown, M.; Brown, R.; Bryant, J.; Croom, S.; Davis, T.; Driver, S.; Filipovic, M.; Hinton, S.; Johnston-Hollitt, M.; Jones, H.; Koribalski, B.; Kleiner, D.; Lawrence, J.; Lorente, N.; Mould, J.; Owers, M.; Pimblet, K.; Tinney, C.; Tothill, N.; Watson, F. The Taipan galaxy survey: Scientific goals and observing strategy. *Publ. Astron. Soc. Aust.* **2017**, *34*.
- [5] Cirasuolo, M.; Afonso, J.; Carollo, M.; Flores, H.; Maiolino, R.; Oliva, E.; Paltani, S.; Vanzi, L.; Evans, C.; Abreu, M.; Atkinson, D.; Babusiaux, C.; Beard, S.; Bauer, F.; Bellazzini, M.; Bender, R.; Best, P.; Bezawada, N.; Bonifacio, P.; Bragaglia, A.; Bryson, I.; Busher, D.; Cabral, A.; Caputi, K.; Centrone, M.; Chemla, F.; Cimatti, A.; Cioni, M.; Clementini, G.; Coelho, J.; Crnojevic, D.; Daddi, E.; Dunlop, J.; Eales, S.; Feltzing, S.; Ferguson, A.; Fisher, M.; Fontana, A.; Fynbo, J.; Garilli, B.; Gilmore, G.; Glauser, A.; Guinouard, I.; Hammer, F.; Hastings, P.; Hess, A.; Ivison, R.; Jagourel, P.; Jarvis, M.; Kaper, L.; Kauffman, G.; T., A.; Lawrence, A.; Lee, D.; Lemasle, B.; Licausi, G.; Lilly, S.; Lorenzetti, D.; Lunney, D.; Mannucci, F.; McLure, R.; Minniti, D.; Montgomery, D.; Muschelok, B.; Nandra, K.; Navarro, R.; Norberg, P.; Oliver, S.; Origlia, L.; Padilla, N.; Peacock, J.; Pedichini, F.; Peng, J.; Pentericci, L.; Pragt, J.; Puech, M.; Randich, S.; Rees, P.; Renzini, A.; Ryde, N.; Rodrigues, M.; Roseboom, I.; Royer, F.; Saglia, R.; Sanchez, A.; Schiavon, R.; Schnetler, H.; Sobral, D.; Speziali, R.; Sun, D.; Stuik, R.; Taylor, A.; Taylor, W.; Todd, S.; Tolstoy, E.; Torres, M.; Tosi, M.; Vanzella, E.; Venema, L.; Vitali, F.; Wegner, M.; Wells, M.; Wild, V.; Wright, G.; Zamorani, G.; Zoccali, M. Moons: The multi-object optical and near-infrared spectrograph for the Vlt. *Proc. SPIE*. **2014**, *9147*, 9147–9147.
- [6] Depagne, A.; Miglio, A.; Eggenberger, P.; Girardi, L.; Montalbán, J. 4most: 4m multi object spectroscopic telescope. In *Asteroseismology of stellar populations in the milky way, astrophysics and space science proceedings*. Cham: Springer International Publishing; pp. 147–154.
- [7] Aghamousa, A.; Aguilar, J.; Ahlen, S.; Alam, S.; Allen, L.; Prieto, C.; Annis, J.; Bailey, S.; Balland, C.; Ballester, O.; Baltay, C.; Beaufore, L.; Bebek, C.; Beers, T.; Bell, E.; Bernal, J.; Besuner, R.; Beutler, F.; Blake, C.; Bleuler, H.; Blomqvist, M.; Blum, R.; Bolton, A.; Briceno, C.; Brooks, D.; Brownstein, J.; Buckley-Geer, E.; Burden, A.; Burtin, E.; Busca, N.; Cahn, R.; Cai, Y.; Cardiel-Sas, L.; Carlberg, R.; Carton, P.; Casas, R.; Castander, F.; Cervantes-Cota, J.; Claybaugh, T.; Close, M.; Coker, C.; Cole, S.; Comparat, J.; Cooper, A.

- Cousinou, M.; Croce, M.; Cuby, J.; Cunningham, D.; Davis, T.; Dawson, K.; de-la-Macorra, A.; de-Vicente, J.; Delubac, T.; Derwent, M.; Dey, A.; Dhungana, G.; Ding, Z.; Doel, P.; Duan, Y.; Ealet, A.; Edelstein, J.; Eftekhazadeh, S.; Eisenstein, D.; Elliott, A.; Escoffier, S.; Evatt, M.; Fagrellius, P.; Fan, X.; Fanning, K.; Farahi, A.; Farihi, J.; Favole, G.; Feng, Y.; Fernandez, E.; Findlay, J.; Finkbeiner, D.; Fitzpatrick, M.; Flaugher, B.; Flender, S.; Font-Ribera, A.; Forero-Romero, J.; Fosalba, P.; Frenk, C.; Fumagalli, M.; Gaensicke, B.; Gallo, G.; Garcia-Bellido, J.; Gaztanaga, E.; Fusillo, N.; Gerard, T.; Gershkovich, I.; Giannantonio, T.; Gillet, D.; Gonzalez-de-Rivera, G.; Gonzalez-Perez, V.; Gott, S.; Graur, O.; Gutierrez, G.; Guy, J. The DESI experiment part I: Science, targeting, and survey design. *arXiv*. **2016**, 1611.00036.
- [8] Sugai, H.; Tamura, N.; Karoji, H.; Shimono, A.; Takato, N.; Kimura, M.; Ohyama, Y.; Ueda, A.; Aghazarian, H.; Arruda, M.; Barkhouser, R.; Bennett, C.; Bickerton, S.; Bozier, A.; Braun, D.; Bui, K.; Capocasale, C.; Carr, M.; Castilho, B.; Chang, Y.; Chen, H.; Chou, C.; Dawson, O.; Dekany, R.; Ek, E.; Ellis, R.; English, R.; Ferrand, D.; Ferreira, D.; Fisher, C.; Golebiowski, M.; Gunn, J.; Hart, M.; Heckman, T.; Ho, P.; Hope, S.; Hovland, L.; Hsu, S.; Hu, Y.; Huang, P.; Jaquet, M.; Karr, J.; Kempenaar, J.; King, M.; Fevre, O.; Mignant, D.; Ling, H.; Loomis, C.; Lupton, R.; Madec, F.; Mao, P.; Marrara, L.; Menard, B.; Morantz, C.; Murayama, H.; Murray, G.; Oliveira, A.; Oliveira, C.; Oliveira, L.; Orndorff, J.; Vilaca, R.; Partos, E.; Pascal, S.; PegotOgier, T.; Reiley, D.; Riddle, R.; Santos, L.; Santos, J.; Schwochert, M.; Seiffert, M.; Smee, S.; Smith, R.; Steinkraus, R.; Sodre, L.; Spergel, D.; Surace, C.; Tresse, L.; Vidal, C.; Vives, S.; Wang, S.; Wen, C.; Wu, A.; Wyse, R.; Yan, C. Prime focus spectrograph for the Subaru telescope: Massively multiplexed optical and near-infrared fiber spectrograph. *J. of Astronomical Telescopes, Instruments, and Systems*, 1(3) 035001, 2015.
- [9] Rogers, K.; Stuijk, R.; Steele, I.; Pragt, J.; Middleton, K.; Bates, S.; Kragt, J.; Tromp, N.; Lesman, D.; Lhome, E.; Dalton, G.; Trager, S.; Navarro, R.; Abrams, D.; Tosh, I.; Jasko, A.; Martin, C.; Mahony, N.; Pico, S.; Infantes, D.; Bianco, A.; Delgado, J.; Rodriguez, L. The design of the weave spectrograph. *Proc. SPIE*. **2014**, 9147, 9147–9147.
- [10] Lewis, I.J.; Dalton, G.B.; Brock, M.; Gilbert, J.; Abrams, D.; Aguerri, J.; Bonifacio, P.; Middleton, K.; Trager, S. Fibre positioning concept for the weave spectrograph at the WHT. Vol. 9147. In *Modern technologies in space- and ground-based telescopes and instrumentation*. SPIE, Proc.2014; 914734.
- [11] Gilbert, J.; Dalton, G. Echidna Mark II: One giant leap for 'tilting spine' fibre positioning technology. In *Modern technologies in space- and ground-based telescopes and instrumentation*, Proc.SPIE. 2016, 9912
- [12] Akiyama, M.; Smedley, S.; Gillingham, P.; Brzeski, J.; Farrell, T.; Kimura, M.; Muller, R.; Tamura, N.; Takato, N. Performance of Echidna fiber positioner for FMOS on Subaru. Vol. 7018. In *Modern technologies in space- and ground-based telescopes and instrumentation*. SPIE, 2008. 70182V.
- [13] Gilbert, J.; Goodwin, M.; Heijmans, J.; Muller, R.; Miziarski, S.; Brzeski, J.; Waller, L.; Saunders, W.; Bennet, A.; Tims, J. Starbugs: All-singing, all-dancing fibre positioning robots. Vol. 8450. In *Modern technologies in space- and ground-based telescopes and instrumentation*. SPIE, 2012, 84501A–84501A–14.
- [14] Goodwin, M.; Heijmans, J.; Saunders, I.; Brzeski, J.; Saunders, W.; Muller, R.; Haynes, R.; Gilbert, J. Starbugs: Focal plane fiber positioning technology. Vol. 7739. In *Modern technologies in space- and ground-based telescopes and instrumentation*. Proc.SPIE. 2014, 7739, 77391E
- [15] Kronig, L.; Hoerler, P.; Bleuler, H.; Bourl, M.; Kneib, J-P. Herausforderungen in design und kalibration für hoch-präzise mikroroboter für spektroskopie messungen von galaxien. *IFTtoMM D-A-CH Konferenz*. 5th edition **2019**.
- [16] Montgomery, D.; Atkinson, D.; Beard, S.; Cochrane, W.; Drass, H.; Guinouard, I.; Lee, D.; Taylor, W.; Rees, P.; Watson, S. Development of the fibre positioning unit of moons. *Proc.SPIE*. **2016**, 9908, 9908–9908–15.
- [17] Fisher, C.; Morantz, C.; Braun, D.; Seiffert, M.; Aghazarian, H.; Partos, E.; King, M.; Hovland, L.E.; Schwochert, M.; Kaluzny, J.; Capocasale, C.; Houck, A.; Gross, J.; Reiley, D.; Mao, P.; Riddle, R.; Bui, K.; Henderson, D.; Haran, T.; Culhane, R.; Piazza, D.; Walkama, E. Developing engineering model cobra fiber positioners for the Subaru telescope's prime focus spectrometer. *Proc.SPIE*. **2014**, 9151, 91511Y.
- [18] Fisher, C.D.; Braun, D.F.; Kaluzny, J.V.; Seiffert, M.D.; Dekany, R.G.; Ellis, R.S.; Smith, R.M. Developments in high-density cobra fiber positioners for the Subaru telescope's prime focus spectrometer. *Proc. SPIE*. **2012**, 8450, 845017.
- [19] Schubnell, M.; Ameel, J.; Besuner, R.; Gershkovich, I.; Hoerler, P.; Kneib, J.; Heetderks, H.; Silber, J.; Tarle, G.; Weaverdyck, C. The desi fiber positioner system. *Proc.SPIE*. **2016**, 9908, 9908 – 9908 – 6.
- [20] Leitner, D.; Aguilar, J.; Ameel, J.; Besuner, R.; Claybaugh, T.; Heetderks, H.; Schubnell, M.; Kneib, J.; Silber, J.; Tarle, G.; Weaverdyck, C.; Zhang, K. Dark energy spectroscopic instrument (Desi) fiber positioner production. *Proc.SPIE*. **2018**, 10706, 10706 – 10706 – 9
- [21] Kollmeier, J.A.; Zasowski, G.; Rix, H.; Johns, M.; Anderson, S.; Drory, N.; Johnson, J.; Pogge, R.; Bird, J.; Blanc, G.; Brownstein, J.; Crane, J.; De-Lee, N.; Klaene, M.; Kreckel, K.; MacDonald, N.; Merloni, A.; Ness, M.; O'Brien, T.; Sanchez-Gallego, J.; Sayres, C.; Shen, Y.; Thakar, A.; Tkachenko, A.; Aerts, C.; Blanton, M.; Eisenstein, D.; Holtzman, J.; Maoz, D.; Nandra, K.; Rockosi, C.; Weinberg, D.; Bovy, J.; Casey, A;

- Chaname, J.; Clerc, N.; Conroy, C.; Eracleous, M.; Gaensicke, B.; Hekker, S.; Horne, K.; Kauffmann, J.; McQuinn, K.; Pellegrini, E.; Schinnerer, E.; Schlafly, E.; Schwobe, A.; Seibert, M.; Teske, J.; van-Saders, J. SDSS-V: Pioneering panoptic spectroscopy. *arXiv*. **2017**.
- [22] Hörler, P.; Kronig, L.; Kneib, J.-P.; Bouri, M.; Bleuler, H.; von Moos, D. High density fiber positioner system for massive spectroscopic surveys. *Month. Not. Royal Astronom. Soc.* **2018**, *481*, 3070–3082.
- [23] Hörler, P.; Kronig, L.; Kneib, J.-P.; Bleuler, H.; Bouri, M. A 24mm diameter fibre positioner for spectroscopic surveys. *Proc.SPIE*. **2016**, *9912*, 99125K.
- [24] Fahim, N.; Prada, F.; Kneib, J.P.; Glez-de-Rivera, G.; Hörler, P.; Sánchez, J.; Azzaro, M.; Becerril, S.; Bleuler, H.; Bouri, M.; Castano, J.; Garrido, J.; Gillet, D.; Gomez, C.; Gomez, M.; Gonzalez-Arroyo, A.; Jenni, L.; Makarem, L.; Yepes, G.; Arrillaga, X.; Carrera, M.; Diego, R.; Charif, M.; Hug, M.; Lachat, C. An 8-mm diameter fibre robot positioner for massive spectroscopy surveys. *Month. Not. Royal Astronom. Soc.* **2015**, *450*, 794794–794806.
- [25] Silber, J.H.; Schenk, C.; Anderssen, E.; Bebek, C.; Becker, F.; Besuner, R.; Cepeda, M.; Edelstein, J.; Heetderks, H.; Jelinsky, P.; Johnson, T.; Karcher, A.; Perry, P.; Post, R.; Sholl, M.; Wilson, K.; Zhou, Z. Design and performance of an r-theta fiber positioner for the Bigboss instrument. *Proc.SPIE*. **2012**, *8450*, 38.
- [26] Kronig, L.; Hörler, P.; Caseiro, S.; Grossen, L.; Araujo, R.; Kneib, J.-P.; Bouri, M. Optical test procedure for characterization and calibration of robotic fiber positioners for multiobject spectrographs. *J. Astron. Telesc. Instrum. Syst.* **2020**, *6*, 1–21.
- [27] Hörler, P. Robotic fiber positioning systems for massive spectroscopic surveys: Mechanical design guidelines and technological opportunities. 2018, *PhD THESIS EPFL*
- [28] Pérez-Calpena, A.; Mancera, E.; Gomez-Alvarez, P.; Delgado, I.; Castillo, A.; Gil-de-Paz, A.; Arrillaga, X.; Vargas, M.; Gallego, J.; Licea, E.; Iglesias-Paramo, J.; Cedazo, R. Megara Mos: Where are my positioners and fibers pointing to? *Proc. SPIE*. **2018**, *10706*, 20
- [29] Zhang, K.; Silber, J.; Heetderks, H.; Leitner, D.; Schubnell, M.; Levi, M.; Wang, G.; Fanning, K.; Fagreluis, P.; Dobson, C.; Aguilar, J. Dark energy spectroscopic instrument (Desi) fiber positioner thermal and wind disturbance test. *Proc. SPIE*. **2018**, *10706*, 12.
- [30] Schubnell, M.; Aguilar, J.; Ameel, J.; Caseiro, S.; Fanning, K.; Freudenstein, B.; Gershkovich, I.; Heetderks, H.; Hoerler, P.; Leitner, D.; Levi, M.; Silber, J.; Sun, Z.; Tarle, G.; Weaverdyck, C.; Zhang, K.; Brooks, D. DESI fiber positioner testing and performance (Conference Presentation). Vol. 1070. In *Advances in optical and mechanical technologies for telescopes and instrumentation III*; International Society for Optics and Photonics, SPIE, 2018. 107062A
- [31] Taylor, W.; Cirasuolo, M.; Afonso, J.; Carollo, M.; Evans, C.; Flores, H.; Maiolino, R.; Paltani, S.; Vanzi, L.; Abreu, M.; Amans, J.; Atkinson, D.; Barrett, J.; Beard, S.; Béchet, C.; Black, M.; Boettger, D.; Brierley, S.; Buscher, D.; Cabral, A.; Cochran, W.; Coelho, J.; Colling, M.; Conzelmann, R.; Dalesio, F.; Dauvin, L.; Davidson, G.; Drass, H.; Dünner, R.; Fairley, A.; Fasola, G.; Ferruzzi, D.; Fisher, M.; Flores, M.; Garilli, B.; Gaudemard, J.; Gonzalez, O.; Guinouard, I.; Gutierrez, P.; Hammersley, P.; Haignon, R.; Haniff, C.; Hayati, M.; Ives, D.; Iwert, O.; Laporte, P.; Lee, D.; Li, G.; Luco, Y.; Macleod, A.; Mainieri, V.; Maire, C.; Melse, B.; Nix, J.; Oliva, E.; Oliveira, A.; Origlia, L.; Parry, I.; Pedichini, F.; Piazzesi, R.; Rees, P.; Reix, F.; Rodrigues, M.; Rojas, F.; Rota, S.; Royer, F.; Santos, P.; Schnell, R.; Shen, T.; Sordet, M.; Strachan, J.; Sun, X.; Tait, G.; Torres, M.; Tozzi, A.; Tulloch, S.; Valenzuela, A.; Von, L.; Waring, C.; Watson, S.; Woodward, B.; Yang, Y. Rising moons: An update on the Vlt's next multi-object spectrograph as it begins to grow. *Proc. SPIE*. **2018**, *10702*, 20
- [32] Gu, Y.; Xu, J.; Jin, Y.; Zhai, C. A high-resolution measurement device for detecting the positioning accuracy of the optical fiber positioner. *Proc. SPIE*. **2012**, *8450*, 84503B.
- [33] Kronig, L.; Hörler, P.; Kneib, J.-P.; Bouri, M. Design and performances of an optical metrology system to test position and tilt accuracy of fiber positioners. *Proc. SPIE*. **2018**, *10706*, 7.
- [34] Tao, D.; Makarem, L.; Bouri, M.; Kneib, J.-P.; Gillet, D. Priority coordination of fiber positioners in multi-objects spectrographs. *Proc. SPIE*. **2016**, *10702*, 2639–2652.
- [35] Makarem, L.; Kneib, J.-P.; Gillet, D.; Bleuler, H.; Bouri, M.; Jenni, L.; Prada, F.; Sanchez, J. Collision avoidance in next-generation fiber positioner robotic systems for large survey spectrographs. *A&A*. **2014**, *566*, A84.
- [36] Macktoobian, M.; Gillet, D.; Kneib, J.-P. Complete coordination of robotic fiber positioners for massive spectroscopic surveys. *J. Astron. Telesc. Instrum. Syst.* **2019**, *5*, 1.
- [37] Macktoobian, M.; Gillet, D.; Kneib, J.-P. Optimal target assignment for massive spectroscopic surveys. *Astron. Comput.* **2020**, *30*, 100364. DOI: [10.1016/j.ascom.2020.100364](https://doi.org/10.1016/j.ascom.2020.100364).
- [38] Lyshevski, S. *Electromechanical systems, electric machines, and applied mechatronics*. 1st edition. CRC Press/Taylor & Francis, Boca Raton, FL, 1999.